

Electronic Thesis and Dissertation Repository

---

1-12-2018 12:00 PM

## Embedded Smart-Polymer Sensor Arrays for Elucidating Load Distributions in Orthopaedic Implants

Carolina Micolini, *The University of Western Ontario*

Supervisor: Price, Aaron D., *The University of Western Ontario*

Co-Supervisor: Johnson, Jim A., *The University of Western Ontario*

A thesis submitted in partial fulfillment of the requirements for the Master of Engineering Science degree in Biomedical Engineering

© Carolina Micolini 2018

Follow this and additional works at: <https://ir.lib.uwo.ca/etd>



Part of the [Biomedical Devices and Instrumentation Commons](#)

---

### Recommended Citation

Micolini, Carolina, "Embedded Smart-Polymer Sensor Arrays for Elucidating Load Distributions in Orthopaedic Implants" (2018). *Electronic Thesis and Dissertation Repository*. 5200.  
<https://ir.lib.uwo.ca/etd/5200>

This Dissertation/Thesis is brought to you for free and open access by Scholarship@Western. It has been accepted for inclusion in Electronic Thesis and Dissertation Repository by an authorized administrator of Scholarship@Western. For more information, please contact [wlsadmin@uwo.ca](mailto:wlsadmin@uwo.ca).

## Abstract

The long-term outcomes of orthopaedic joint implants are only beginning to be understood, making it imperative to monitor the contact loads across the entire implant interface. This capability will elucidate the force transmission and distribution mechanisms exhibited by these implants in-service over time. This study explores the design and implementation of 3D-printed smart-polymer force sensor arrays, consisting of piezoresistive polyaniline (PANI) structures embedded within a polymeric parent phase. This unique multi-material additive manufacturing process was then employed to realize transducers embedded in the humeral component of a replacement prosthetic device conventionally used to restore the functionality of the shoulder joint. Ultimately, implant designers that better understand the interface loads can combat the wear and loosening of these prosthetics early on, reducing the number of design revisions required and increasing the longevity of the implants.

**Keywords:** intrinsically conductive polymers, piezoresistance, polyaniline, sensing array, orthopaedic joint implants, reverse total shoulder arthroplasty, conjugated polymers

A person can never be broken. Our built environment, our technologies are broken and disabled. We the people need not accept our limitations, but can transcend disability through technological innovation.

– Hugh Herr

Prof. of Media Arts and Sciences

Massachusetts Institute of Technology, 2014

## **Dedication**

A mis padres, por abrirme las puertas al Mundo.

A mi amor, por acompañarme a recorrerlo.

# Acknowledgements

Financial support for my graduate studies was generously provided by the Organization of American States through the “OAS Regular Program for Academic Scholarships (Graduate),” and the University of Western Ontario.

I would like to extend my thanks to the members of my Examination Committee, and in particular to Prof. Ana Luisa Trejos for her guidance throughout the duration of this project. I would also like to acknowledge the insightful guidance of my co-supervisor, Prof. Jim Johnson. I am grateful for his support in the field of Biomechanics, and for guiding my steps towards the world of Biomedical Engineering. Additionally, I would like to thank Dave Lunn for his time and valuable assistance.

I would also like to express my sincere gratitude to my thesis supervisor Prof. Aaron Price for his continual support, and demonstrating a contagious love for academia and research. Your passion for the search for knowledge and the love that you profess to your family and colleagues is truly admirable. Thank you for being a great role model.

Special thanks also to my colleagues in the Organic Mechatronics and Smart Materials Laboratory, especially Benjamin Holness, for sharing your knowledge with me. Thanks to the International and Exchange Student Centre, and to all my international friends, for being my home away from home during my stay in Canada.

On a personal note, I would like to show my heartfelt appreciation for my friends and family who lovingly support me in all of my endeavours. I owe special gratitude to the love of my life, Franco, for following me to the other end of our continent, and for always being optimistic and cheerful towards life, to my brother for showing me that it is possible to achieve our dreams, and finally, thank you to my Parents for opening the doors of the World to me.

Every person I have met along every step of the way has opened my eyes to a new reality and has enriched my world. I will always be grateful to you all.

# Contents

<b>Contents</b>	<b>vi</b>
<b>List of Tables</b>	<b>x</b>
<b>List of Figures</b>	<b>xi</b>
<b>List of Acronyms and Symbols</b>	<b>xiii</b>
<b>1 Introduction</b>	<b>1</b>
1.1 Objectives . . . . .	2
1.2 Major contributions . . . . .	3
1.3 Organization of the thesis . . . . .	4
List of references . . . . .	5
<b>2 Background</b>	<b>7</b>
2.1 Polyaniline . . . . .	7
2.1.1 Piezoresistive effect . . . . .	8
2.1.2 Sensing modalities . . . . .	10
2.2 Joint force measurement in orthopaedic implants . . . . .	11
2.2.1 Significance of measurements . . . . .	11
2.2.2 Different approaches for joint force measurement . . . . .	12
2.2.3 An exciting application: total reverse shoulder arthroplasty . . . . .	14

2.3	Chapter summary . . . . .	17
	List of references . . . . .	17
<b>3</b>	<b>Design and performance of a pressure sensor arrays</b>	<b>24</b>
3.1	Design and fabrication . . . . .	24
3.1.1	Substrate material selection . . . . .	25
3.1.2	Sensor design . . . . .	26
3.1.3	3D-printing . . . . .	26
3.1.4	Methods for wire connection . . . . .	27
3.2	Signal acquisition and processing . . . . .	27
3.2.1	Temperature compensation . . . . .	30
3.3	Calibration apparatus . . . . .	31
3.4	Chapter summary . . . . .	32
	List of references . . . . .	33
<b>4</b>	<b>Planar sensor array characterization</b>	<b>34</b>
4.1	Design and fabrication . . . . .	34
4.1.1	Sensor design . . . . .	34
4.1.2	3D-printing . . . . .	35
4.1.3	Thermal treating and wiring . . . . .	37
4.2	Calibration apparatus . . . . .	38
4.3	Performance characterization . . . . .	38
4.3.1	Stability . . . . .	39
4.3.2	Cyclic loading . . . . .	39
4.3.3	Incremental continuous loading . . . . .	40
4.3.4	Incremental loading: zero breaks . . . . .	40
4.3.5	Loading/unloading cycle . . . . .	41
4.3.6	Repeatability . . . . .	41

4.3.7	Precision . . . . .	41
4.4	Results . . . . .	42
4.4.1	Stability . . . . .	42
4.4.2	Cyclic loading . . . . .	43
4.4.3	Incremental continuous loading . . . . .	43
4.4.4	Incremental loading: zero breaks . . . . .	44
4.4.5	Loading/unloading cycle . . . . .	44
4.4.6	Repeatability . . . . .	45
4.4.7	Precision . . . . .	45
4.5	Discussion . . . . .	48
4.6	Chapter summary . . . . .	50
	List of references . . . . .	51
<b>5</b>	<b>Application in an orthopaedic implant</b>	<b>52</b>
5.1	Design and fabrication . . . . .	52
5.1.1	Sensor design . . . . .	53
5.1.2	3D-Printing and PANI deposition . . . . .	53
5.1.3	Wiring and thermal treating . . . . .	55
5.2	Adaptation of the calibration apparatus . . . . .	56
5.3	Performance characterization . . . . .	57
5.3.1	Cyclic loading . . . . .	58
5.3.2	Stability . . . . .	59
5.3.3	Incremental continuous loading of individual elements . . . . .	59
5.3.4	Incremental continuous loading of the entire sensor . . . . .	60
5.4	Signal acquisition and processing . . . . .	61
5.5	Results . . . . .	61
5.5.1	Cyclic loading . . . . .	62
5.5.2	Stability . . . . .	63



5.5.3	Incremental continuous loading of individual elements . . . . .	63
5.5.4	Incremental continuous loading of the entire sensor . . . . .	64
5.6	Signal acquisition and processing . . . . .	66
5.7	Discussion . . . . .	68
5.8	Chapter summary . . . . .	71
	List of references . . . . .	71
<b>6</b>	<b>Concluding remarks</b>	<b>73</b>
6.1	Summary of conclusions . . . . .	73
6.2	Summary of contributions . . . . .	75
6.3	Recommendations for future research . . . . .	76
	<b>Appendices</b>	<b>78</b>
<b>A</b>	<b>Curriculum vitæ</b>	<b>79</b>

# List of Tables

4.1	$R^2$ values for the linear fitting of sensor output. . . . .	45
4.2	Root Mean Square (RMS) Error . . . . .	48

# List of Figures

2.1	PANI Emeraldine forms . . . . .	8
2.2	Diagram showing RTSA and shoulder bone anatomy . . . . .	15
2.3	Conceptual representation of concentration of forces in the humeral cup	17
3.1	Modified fused filament fabrication delta robot . . . . .	26
3.2	Schematic connection for one PANI element . . . . .	28
3.3	Test mode GUI . . . . .	29
3.4	Flat sensor mode GUI . . . . .	30
3.5	Calibration apparatus . . . . .	31
3.6	Schematic of setup for piezoresistive characterization . . . . .	32
4.1	Conceptual representation of embedded sensor in orthopaedic implant .	35
4.2	CAD illustration of the flat sensor . . . . .	36
4.3	Screen capture generated by Simplify3D of the printing pattern . . . . .	37
4.4	3D-printed sensor array without the wires - front and back view . . . . .	37
4.5	Schematic of the flat sensor's setup for piezoresistive characterization .	38
4.6	Change in resistance under no load and continuous load . . . . .	43
4.7	Fractional change in unloaded-resistance as a function of cyclic loading .	44
4.8	Fractional change in loaded-resistance as a function of cyclic loading . .	45
4.9	Linear fits for the change in resistance during incremental loading . . . . .	46
4.10	Linear fits for the change in resistance during loading-zero breaks . . . . .	46

4.11	Relative change in resistance on Element #4 during loading/unloading . . . . .	47
4.12	Change in resistance on Element #4 during loading . . . . .	47
5.1	CAD illustration of the humeral cup sensor . . . . .	54
5.2	CAD illustration of the humeral cup cover . . . . .	55
5.3	Wiring and PANI embedment procedure for the curved sensor . . . . .	56
5.4	Calibration apparatus for testing individual elements of the curved sensor	57
5.5	Calibration apparatus for joint testing of the curved sensor . . . . .	61
5.6	Fractional change in unloaded-resistance under cyclic loading . . . . .	62
5.7	Fractional change in loaded-resistance under cyclic loading . . . . .	63
5.8	Change in resistance under continuous load . . . . .	64
5.9	Change in resistance for element (#1) during incremental loading . . . . .	65
5.10	Change in resistance for element (#13) during incremental loading . . . . .	65
5.11	Change in resistance for element (#11) during incremental loading . . . . .	66
5.12	Change in resistance during incremental loading at 0° . . . . .	67
5.13	Custom GUI for displaying measurements from the 3D sensor . . . . .	68

# List of Acronyms and Symbols

## Acronyms

ABS	Acrylonitrile butadiene styrene
CNT	Carbon nanotube
COP	Conductive organic polymer
CP	Conductive polymer
CSA	Camphor sulfonic acid
CT	Computed tomography
DAQ	Data acquisition
DBSA	Dodecylbenzene sulfonic acid
ES	Emeraldine salt
GF	Gauge factor
GUI	Graphical user interface
HMA	Hot melt adhesive
PANI-Cl	Hydrochloric polyaniline
PANI	Polyaniline
PDMS	Polydimethylsiloxane
PLA	Poly(lactic acid)
RMS	Root mean square
RMSE	Root mean square error
RTSA	Total reverse shoulder arthroplasty

SEBS	Styrene ethylene butadiene styrene
TPE	Thermoplastic elastomer
TSA	Total shoulder arthroplasty
UHMWPE	Ultra-high molecular weight polyethylene
U.S.	United States

### **Greek symbols**

$\epsilon$	Mechanical strain
$\nu$	Poisson's ratio
$\rho$	Resistivity

### **Latin symbols**

$\Delta l$	Applied deformation
$\Delta R/R_0$	Fractional change in resistance
$R$	Variable PANI resistance measured
$R_0$	Value for the unloaded-resistance measured
$R_{20\%}$	Value for the loaded-resistance at 20% of the air compressor input
$R_{5\%}$	Value for the loaded-resistance at 5% of the air compressor input
$R_{\text{PANI}}$	Variable PANI element resistance measured
$R_S$	Shunt resistor
$V_{in}$	Input voltage
$V_R$	Voltage drop across $R$

# Chapter 1

## Introduction

Like many great scientific discoveries, conductive polymers were discovered accidentally. Between the years of 1960 and 1970, three professors: Alan J. Heeger from the University of California, USA; Alan G. MacDiarmid from the University of Pennsylvania, USA; and Hideki Shirakawa from the University of Tsukuba in Japan, were all separately investigating the potential conductivity of polymers. In 1975, after a decade of independent research, Prof. Heeger, Prof. MacDiarmid and Prof. Shirakawa finally came together to collaborate. Only a year after first meeting, they observed, for the first time in history, the “doping” effect in conducting polymers (Wan, 2008). In 2000, this discovery won them the Nobel Prize in Chemistry “for the discovery and development of conductive polymers” (Nobel Media, 2017).

While polymers were only discovered a few decades ago, the medical specialty of orthopaedics can be traced back to the origins of human civilization. However, it was only in 1741, when Nicolas Andry published his book *Orthopédie* or the “art of correcting and preventing deformities in children” (Andry, 1741), that the term “orthopaedics” was created, and not until 1780, when Jean-André Venel opened the first orthopaedic Hospital of the World in Switzerland (Di Matteo et al., 2013), that the word was widely used. Although the term orthopaedic initially described the treatment of skeletal defor-

mities in children, the definition quickly evolved within the medical field to describe the treatment, prevention and/or correction of any bone or joint deformation of the body.

This study focuses on orthopaedic implants that are mainly used for joint replacement. This type of implant improves the quality of life for those individuals suffering from arthritis or other various diseases that reduce the functionality of joints (Revell, 2014). Since the early uses of orthopaedic implantations, scientists have investigated their wear patterns, failure modes, longevity, as well as how the materials of the implant interact with each other and how they act among the living cells in the body when implanted (Wang et al., 2011). Since this type of implant impacts such a wide range of people, it is beneficial to continuously improve upon its design.

Over the years, scientists have tried to use conductive polymers in different applications, using pressure sensors as the main mode of investigation. More recently, a conductive organic polymer (COP) called Polyaniline (PANI), was proven to be biocompatible (Mattioli-Belmonte et al., 2003), making it suitable for pressure sensor applications in orthopaedic implants. This study focusses on joint replacement implants, specifically those that use Ultra-High Molecular Weight Polyethylene (UHMWPE) components; a material introduced in the 1960s as a bearing component in hip replacements by Dr. Charnley (Musib, 2011). It has been proven that the forces supported by orthopaedic implants directly impact the wear of these UHMWPE components (D'Lima et al., 2012). By embedding the COP sensing element into the implant, the modifications to the internal structure of the implant may be reduced, possibly leading to more accurate measurements of the internal loads.

## 1.1 Objectives

This research project aims to make use of the piezoresistive property of polyaniline for pressure sensing elements, within the fabrication of 3D-printed implant components



that are embedded with smart-polymer sensors. This main objective is divided into the following research objectives:

- *Establish the feasibility and performance characteristics of embedded 3D-printed smart-polymer stress sensor arrays in a planar geometry.* The first objective is to study the piezoresistive characteristics of PANI to characterize the sensing behaviours inherent to these embedded pressure sensor arrays. To carry this out, a unique calibration apparatus will be designed to perform compression tests. A software interface will also be developed to analyze the voltage signal and to calculate the resistance of PANI. Finally, a combination of the characteristics and precision of PANI's stable response to a continuous load, stability throughout loading and unloading cycles, and repeatable and linear responses to incremental loading cycles will be investigated.
- *Extend this concept to similar geometries of a typical joint replacement implant.* The second objective is to fabricate a curved sensor that mimics the humeral cup of a reverse total shoulder arthroplasty implant. The calibration apparatus will be modified to accommodate for the geometry of the humeral component of these implants, so that a force perpendicular to each PANI element can be applied at the time of the calibration. In addition, the custom-made software interface will be modified to calibrate each PANI element individually. Finally, a graphical user interface will be developed to display the sensed forces.

## **1.2 Major contributions**

This thesis provides the following major contributions to the scientific body of knowledge:

- *Novel 3D-printed smart-polymer stress sensor arrays in a planar geometry.* These

sensor arrays are composed of 3D-printed PANI sensing elements that are embedded in a thermoplastic elastomer. This sensor makes use of PANI's piezoresistive properties to detect load changes during the unidirectional loading of its elements. After calibration, the custom-made software is able to relate the applied load with the corresponding changes in resistance and then plot the data in the graphical user interface.

- *Characterization of the direct-writing of PANI's piezoresistive properties under a unidirectional load.* This is the first study to examine the piezoresistive properties of PANI elements constructed with a novel 3D-printing technique. This study is significant as it relates the resistance changes that PANI presents to the unidirectional loads that are applied to it. This will allow for the manufacturing of diverse pressure sensors within the limits of the linear range.
- *Embedded PANI piezoresistive sensors in orthopaedic joint replacement implants.* The planar geometry was adapted to fit a hemispherical geometry that mimics the typical humeral cup of a reverse total shoulder arthroplasty prosthesis. This adaptation demonstrates one of the many possible applications for this sensor-manufacturing technique that can be used to study different types of prosthetics.

### **1.3 Organization of the thesis**

The following chapter, Chapter 2, *Background*, summarizes the most significant studies on the piezoresistive effect of polyaniline, in order to better understand how to use this feature to develop pressure sensors. In addition, a brief description of the significance of joint force measurements in a joint replacement orthopaedic implant, a relatively new and exciting application of PANI, as well as a description of the most common methods used to measure these forces will be included.

In accordance with the aforementioned objectives, the remainder of the thesis is organized as follows: Chapter 3, *Design and performance of a pressure sensor arrays*, explores different design and fabrication considerations for conductive polymer pressure sensor arrays. Next, Chapter 4, *Planar sensor array characterization*, characterizes polyaniline as a sensing element by means of a 3D-printed flat sensors composed of an  $3 \times 3$  array of PANI rectangular prisms embedded in a flexible polymeric substrate. Chapter 5, *Application in an orthopaedic implant*, extends the knowledge gathered from the fabrication of the flat sensor to the curved sensor used in a joint replacement orthopaedic implant. In addition, the alterations made to the calibration apparatus and the processing and acquisition of the signal will be described. Finally, Chapter 6, *Concluding remarks*, summarizes the primary conclusions of the work, reiterates the main contributions to the knowledge in the biomedical and materials engineering fields, and provides recommendations for future research.

## List of references

- Andry, N. (1741), *L'Orthopédie ou l'art de prévenir et de corriger dans les enfans, les difformités du corps*, Chez La Veuve Alix, Paris.
- Di Matteo, B., Tarabella, V., Filardo, G., Tomba, P., Viganò, A. and Marcacci, M. (2013), 'The "GENESIS" of modern orthopaedics: Portraits of three illustrious pioneers', *International Orthopaedics* **37**(8), 1613–1618.
- D'Lima, D. D., Fregly, B. J., Patil, S., Steklov, N. and Colwell, C. W. (2012), 'Knee joint forces: prediction, measurement, and significance', *Proceedings of the Institution of Mechanical Engineers, Part H: Journal of Engineering in Medicine* **226**(2), 95–102.
- Mattioli-Belmonte, M., Giavaresi, G., Biagini, G., Virgili, L., Giacomini, M., Fini, M., Giantomassi, F., Natali, D., Torricelli, P. and Giardino, R. (2003), 'Tailoring biomaterial

- compatibility: in vivo tissue response versus in vitro cell behavior', *The International journal of artificial organs* **26**(12), 1077–1085.
- Musib, M. K. (2011), 'A Review of the History and Role of UHMWPE as A Component in Total Joint Replacements', *International Journal of Biological Engineering* **1**(1), 6–10.
- Nobel Media (2017), 'The Nobel Prize in Chemistry 2000'.  
**URL:** [nobelprize.org/nobel\\_prizes/chemistry/laureates/2000/](http://nobelprize.org/nobel_prizes/chemistry/laureates/2000/)
- Revell, P. A. (2014), *Joint replacement technology*, 2nd edn, Elsevier Science & Technology, Oxford.
- Wan, M. (2008), *Conducting polymers with micro or nanometer structure*, Springer, New York.
- Wang, W., Ouyang, Y. and Poh, C. K. (2011), 'Orthopaedic implant technology: Biomaterials from past to future', *Annals of the Academy of Medicine Singapore* **40**(5), 237–243.

# Chapter 2

## Background

This chapter provides background information regarding: the study of the piezoresistive effect of PANI, the features of PANI that suggest that it is a plausible candidate in the fabrication of piezoresistive sensors, and the previous sensing modalities that harnessed the piezoresistive property to create pressure sensors. This section will also describe the significant benefits in measuring the joint forces in orthopaedic implant applications. Finally, the most commonly used methods to measure joint reaction forces in orthopaedic implants are presented.

### 2.1 Polyaniline

Polyaniline (PANI), is a conductive organic polymer that has been thoroughly investigated by many researchers and material scientists alike. Features such as its low-cost, ease of synthesis, good environmental stability, in-vitro and in-vivo biocompatibility (Mattioli-Belmonte et al., 2003), and its ability to resist alteration by static charges or external magnetic fields (Kang et al., 2009), all suggest that PANI is a plausible candidate that can be used to fabricate piezoresistive sensors (Adams et al., 1994; Bao et al., 1998; Razak et al., 2016; Falletta et al., 2014; Kang et al., 2009). However, the use of

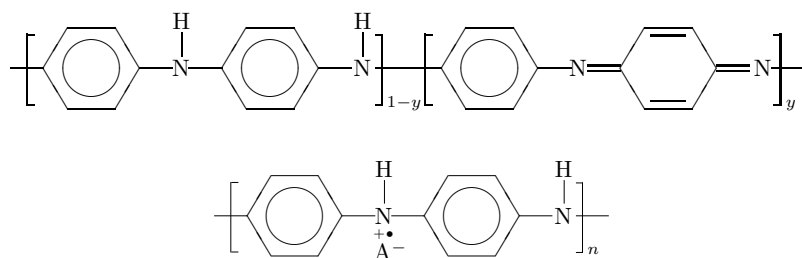


Figure 2.1: Molecular structure of PANI. (**top image**) Insulating undoped Emeraldine base state and (**bottom image**) Conductive doped Emeraldine salt state.

this piezoresistive property inherent in PANI for the manufacturing of sensors, deserves further investigation (Del Castillo-Castro et al., 2012). Polyaniline has three main forms, but it is only electroactive when it is in its half-oxidized/reduced form, known as emeraldine salt (ES) (see Figure 2.1). When pressure is applied to ES, its resistivity changes (Della Pina et al., 2015).

Under compressive loads, the electrical resistance of PANI is reduced, due to the increasing contact of the conducting particles and the re-organization of the electroconductive network structure. It is before the occurrence of any permanent structural damage and when the molecular chains are extremely close together, that the electrical resistance value will be at its lowest. Once the load has been removed and the structure remains undamaged, the resistance will return to its original value. Due to this, PANI is an ideal candidate for the fabrication of piezoresistive sensors (Barra et al., 2008; Bao et al., 1998).

### 2.1.1 Piezoresistive effect

The piezoresistive effect, the property that allows PANI to be used as a sensing element, is a change in the electrical resistivity of a semiconductor when a mechanical strain is applied. Several different approaches have been reported that exploit PANI as a sensing element: Barra et al. (2008) investigated the behaviour of various thermoplastic elastomer/polyaniline blends under compressive stresses, to assess their electrome-

chanical properties and the changes in the conductivity values; Pereira et al. (2012) examined the piezoresistive effect of spin-coated polyaniline thin films; Del Castillo-Castro et al. (2012) studied the piezoresistive responses to compressive loads on composites that used hydrochloric polyaniline (PANI-HCl) as an electrically conducting filler; and Della Pina et al. (2014) compared the electromechanical properties to the compression of the PANI pellets that were obtained by following a green method and a traditional method. Though the studies mentioned all use different approaches for the synthesis, blending, and experimental testing of PANI, the piezoresistive responses of the resulting compounds all suggest that PANI is a good candidate for potential pressure sensor applications.

When studying the piezoresistive effect, another important property to consider is the gauge factor,  $GF$ . This factor is defined as the ratio of relative change in electrical resistance  $R$ , as a function of the mechanical strain, that characterizes the sensitivity of piezoresistive materials (Della Pina et al., 2014). The resistance of PANI changes due to a combination of mechanical deformation and the intrinsic piezoresistive effect, as can be seen in the following equation:

$$GF = \frac{\Delta R/R_0}{\Delta l/l_0} = \frac{d\rho/\rho_0}{\epsilon_l} + 1 + 2\nu, \quad (2.1)$$

where the first term represents the contribution of the intrinsic piezoresistive effect and the second the contribution of the overall shape (Falletta et al., 2014). In this investigation, the PANI has been established to have a  $GF$  that ranges from 6.42 to 5.09. These values exist within the range of the  $GF$  values of commercially available piezoresistive strain sensors (Holness and Price, 2017).

As explained by Bao et al. (1998) and Del Castillo-Castro et al. (2012), the conductivity of PANI can vary depending on the composition, synthesis method, treatment it receives, and experimental conditions. The approach proposed in this thesis uses a

unique combination of these parameters along with a PANI-specific 3D-printing technique (outlined in section 3.1.3) that has the potential to ensure that all of the sensing elements are created uniformly.

### **2.1.2 Sensing modalities**

A wide range of conductive polymers (CPs) utilized in various sensor design applications can be found in the literature (Shtayermman, 2001; Jung et al., 2015; Gau et al., 2009; Hong et al., 2016; Lee et al., 2006; Bae et al., 2004; Nambiar and Yeow, 2011; Castellanos-Ramos et al., 2010). In this section, a variety of state-of-the-art sensors that make use of CPs for pressure sensing will be reviewed.

There are many approaches that harness the properties of CPs and use them for different sensor design applications. For example, Lee et al. (2006) used a capacitive approach with a polydimethylsiloxane (PDMS) elastomer, while Hong et al. (2016) fabricated conductive UHMWPE/PANI composite yarns, and others used different flexible substrates to contain an array of CPs. Different sensor applications were explored by: Jung et al. (2015) who created a sensor composed of a central core and four sidewall structures, fabricated with a carbon nanotube (CNT) mixed with PDMS, that was able to distinguish between the force direction and magnitude; Gau et al. (2009) who found an innovative fabrication method for sensors based on polyimide/CNT nanocomposites in the form of a diaphragm; Bae et al. (2004) who reported a Wheatstone bridge configuration of a CP membrane suspended on a silicon substrate; and Castellanos-Ramos et al. (2010) who worked on a collection of sensors that consisted of a sheet of CP that were piezoresistive on top of a set of electrodes. It is important to note that within these approaches and applications, it was imperative to pay strict attention to the isolation of the sensing elements in order to avoid crosstalk, a phenomenon that occurs when the signal for a single sensing element is impacted by the surrounding sensing elements due to inadequate isolation.



Altogether, all of the manufacturing approaches demonstrated favourable costs, linearity, sensitivity, repeatability, and in some cases, flexibility.

## **2.2 Joint force measurement in orthopaedic implants**

### **2.2.1 Significance of measurements**

Whether it is a shoulder, knee, or hip implant, the motivation for force measurements has always been essentially the same: to understand the differences between the forces exerted on a natural joint and those exerted on artificial joints. When an implant is integrated into the anatomy of the body, a change in the geometry and the mechanical properties of the joint is generated; therefore, the load transfer mechanism and force flow are not expected to match those found in preoperative native anatomy. For this reason, and to broaden the knowledge of the complexity of these systems, it is of particular interest to study the forces transmitted by these implants during different activities of daily life (D'Lima et al., 2001).

The forces supported by implants are directly related to the wear of its components. This is particularly true for Ultra-High Molecular Weight Polyethylene (UHMWPE) components (D'Lima et al., 2012) where the wear of this material has been shown to correlate with contact stresses (D'Lima et al., 2001).

Furthermore, implant designs and surgical techniques are constantly evolving, making it difficult to gather any useful long-term data that could potentially impact future implant designs and their respective patient outcomes (Ackland et al., 2015). A better understanding of the long-term impacts on implants would lead to better clinical outcomes, greater patient satisfaction, and a longer lifespan for the prosthetics.

Recently, using the U.S. Census Bureau's 2014 National Projections, Colby and Ortman (2015) reported that the number of people of the ages of 65 or older in the United States (U.S.) will grow by 9 points; from 15% in 2014 to 24% by 2060. Keeping

this in mind, Hootman et al. (2016) reported that the projected prevalence of arthritis in people over the age of 18 in the U.S., between the years of 2015 to 2040, will increase by 49% (for doctor-diagnosed arthritis) by the year 2040. This increase represents 78.4 million people in the U.S. alone, which is 26% of its total population. In other words, the census projects that in the next 40 years, the 46 million people aged 65 and older, will more than double by the year 2060, meaning a population of 98 million may be affected by arthritis or other joint related conditions. More importantly, Kim et al. (2011) found that the increase in those suffering from arthritis, combined with the growing rate of people over the age of 65, will likely require total reverse shoulder arthroplasty (RSTA) as well as other joint replacements procedures. This increase of people afflicted by arthritis and joint inhibiting conditions will require the fabrication of more prosthetics, therefore a better understanding of their behaviour in the human body can help satisfy the different needs presented by each individual.

### **2.2.2 Different approaches for joint force measurement**

The aim of this study is to implement a new embedded 3D-printed polymer sensor, that uses conductive PANI structures, into a Ultra-High Molecular Weight Polyethylene (UHMWPE) component of a joint replacement orthopaedic prosthesis. The motivation for this design is to elucidate the stress distribution and identify areas of critical wear. Previous efforts have typically used strain gauges to measure the contact load at a discrete point on the surface of the implant, but this only considers the magnitude and not the distribution of the load. In addition, concentrating on a single point can result in wear and plastic deformation of the UHMWPE component (Hong et al., 2016), often leading to failures in inanticipated locations. Therefore, the measurement of loads at discrete points on (or within) the implant is of particular interest as it is important to monitor contact loads across the entire surface area so that force transmission mechanisms encountered by these implants-in-service can be: better understood, used to

create better designs, and increase the longevity of the implants (Smith et al., 2015; Matsen et al., 2008; Nam et al., 2010; Terrier et al., 2008; Berhouet et al., 2014). In addition, the polymers used may enable an approximation of the characteristics of the implant without having to modify the internal structure, leading to a more accurate measurement of the internal loads.

While some specific modifications are made to different types of joint replacement orthopaedic implants, the techniques used to measure the acting forces are, for the most part, similar. Due to this similarity, this study will examine the technique used to estimate the joint loads of a reverse shoulder implant. The two main approaches that can estimate the glenohumeral joint load in reverse shoulder prostheses are: computational modeling and *in vitro* testing of implanted cadaveric shoulders. While the *in vivo* measurement is another method that makes use of instrumented shoulder implants with telemetric data transmission, it was not included because at the time of this thesis, no data was found to confirm that this technique had been used on RTSA (Bergmann et al., 2007).

Each type of testing, whether it be computational or cadaveric, provides a specific set of characteristics and presents its own set of advantages and disadvantages. However, despite the different techniques utilized and the different prostheses analyzed by various authors, in the end, the results resemble each other. As noted by Quental et al. (2015) the simulation of the wear of the implant is incredibly complex due to the number of factors that must be considered. Tashjian et al. (2015) point out that by documenting the specifics regarding the surgical implantation of the prostheses and the anatomy of each patient, a wide range of clinical results can be created. D'Lima et al. (2012) identifies the need to develop an efficient, cost-effective, durable power source as a potential challenge of *in vivo* measurements of knee forces. This is because *in vivo* measurements require powerful data acquisition systems, the capacity to manage bandwidth for real-time data transmission, sufficient storage and efficient data processing capabilities.

In both cadaveric and CT-based computational studies that are based on patient data records, the patient sample was significantly small. As D'Lima et al. (2012) report, it is important to extrapolate data from a larger and more diverse (different age or sex groups) patient population to properly validate results.

When mathematical models are used, many muscles and ligaments must often be simplified due to their complex geometry. This simplification can lead to the generation of inaccurate results. Before in vivo measurement capabilities, two early limitations of computational models included: the inability to predict the increase in glenohumeral contact forces while the arm was raised above the shoulder, and a decrease in peak forces during fast movements. Computational models usually depict the articular fracture, but in vivo measurements, as the ones carried out by Bergmann et al. (2007), show that the coefficient of friction is expected to be an order of magnitude greater than the one estimated with computational methods. This further emphasizes the benefits of in vivo and in vitro methods over computational ones.

### **2.2.3 An exciting application: total reverse shoulder arthroplasty**

An exciting application of the aforementioned technology is the use of embedded transducers within orthopaedic implants, as the load transfer through these devices is poorly understood. An example where RTSA can be beneficial is in the replacement of shoulder reconstruction surgery, which has gained popularity among the aging “baby boomer” population. Total reverse shoulder arthroplasty (RSTA), is a relatively new procedure that has shown promising short-term results for the treatment of glenohumeral arthritis, massive rotator cuff tears, and as a salvage procedure following the failure of unconstrained anatomical total shoulder arthroplasty (Guery et al., 2006; Cheung et al., 2011; Kwon et al., 2010).

The Glenohumeral joint, a ball and socket joint, is formed between the articulation of the rounded humeral head and the rounded socket (glenoid fossa) of the scapula. It is

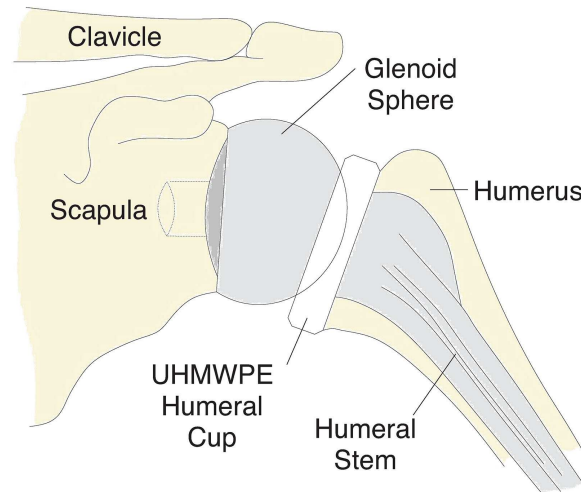


Figure 2.2: Diagram showing the different components of RTSA and the bones of the shoulder.

a joint that lacks strong ligaments, making it muscle-dependent. The primary stabilizers of the shoulder are the biceps brachii and tendons of the rotator cuff, which are fused to all sides of the capsule, except to the inferior margin. The tendons of the rotator cuff and their respective muscles stabilize and fix the joint in place. The rotator cuff is essential for normal shoulder function. When patients obtain massive tears to their rotator cuff, they lose the stability required for the joint and the humeral head slides upwards and begins to move out of the socket. The slackening of the deltoid will cause a poor range of motion of the shoulder while the torn tendons and the subsequent arthritis will cause excruciating pain for the patient.

In reverse total shoulder replacement the articulation is reversed: the articulating head, a spherical cobalt chromium glenoid component, is fixed to the scapula, and the socket, a convex Ultra-High Molecular Weight Polyethylene (UHMWPE) humeral component, is fixed to the upper end of the humerus (see figure Figure 2.2). In patients with a deficient rotator cuff, this construct converts normal shear forces into compressive forces, thereby creating a rotational moment and enabling the deltoid to raise the arm. The area of glenohumeral articulation has greater surface contact following RTSA, which provides inherent joint stability superior to that of an anatomic glenohumeral joint.

The upward pull of the deltoid is neutralized, and the superior translation is eliminated, which enhances stability (Terrier et al., 2008). This concept has proven to be effective to diminish pain and improve function in patients with rotator cuff deficiency (Levigne et al., 2013). The reverse shoulder replacement implant is relatively new, therefore the long-term outcomes are not yet understood. While this procedure has a rate of failure four times higher than anatomical shoulder replacements, it is the only option for cases in which the latter cannot be used (Bohsali, 2006). Total shoulder arthroplasty can also be associated with a multitude of complications, many of which are not fully understood (Martins et al., 2015). The most common of these complications include prosthetic loosening, glenohumeral instability, periprosthetic fracture, rotator cuff tears, infection, neural injury, and deltoid muscle dysfunction (Grammont and Baulot, 2011; Zumstein et al., 2011). However, the RTSA implant designs can be customized to fit the unique set of needs and anatomy of each patient. Some companies that fabricate different types of reverse shoulder implants include: ReUnion® RSA, Depuy Delta XTEND™, Zimmer Trabecular Metal™, Tornier Aequalis Ascend™ Flex, to name a few. In the end, the implant will be made up of components in different configurations at the glenoid or the humerus, to minimize the risks previously discussed.

### **Measurements reported for RTSA**

The joint reaction force reaches the approximate equivalence of half of the body weight of a person (350 N for an average adult male) for a reversed prosthesis (Giles et al., 2015; Kwon et al., 2010; Terrier et al., 2008). Additionally, it has been estimated that the average maximum contact stress, while applying a constant load of 400 N, ranges from 2.28 MPa to 3.28 MPa found for a commercially available 38 mm humeral cup (155° and 145° Neck-Shaft angle, correspondingly), and from 2.1 MPa to 4.48 MPa in a commercially available 42 mm humeral cup (155° and 145° Neck-Shaft angle, correspondingly) (Langohr et al., 2016).

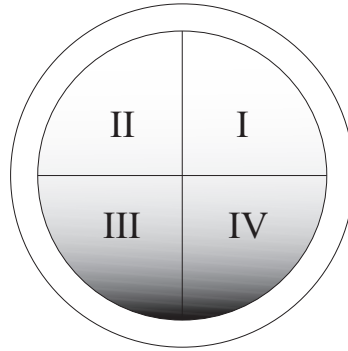


Figure 2.3: Conceptual representation of concentration of forces in the two lower quadrants of the humeral cup (III and IV).

Special emphasis is placed on the study of the lateralization of the center of rotation, to evaluate its effect on load distribution (Costantini et al., 2015; Langohr et al., 2015; Quental et al., 2015). Although all studies show that forces are concentrated in the two lower quadrants of the humeral cup (as seen in Figure 2.3), there is no data that outlines how these forces are distributed within the sensor. Therefore, there is a need to study the distribution of the load within these implants.

## 2.3 Chapter summary

This chapter provides a brief review of the many approaches taken to study PANI as a sensing element. The approaches to employ this feature in pressure sensors have been discussed. The reasoning behind the need to study and understand joint reaction force measurements in UHMWPE implants has been outlined together with a survey of contemporary techniques employed for its measurement.

## List of references

Ackland, D. C., Patel, M. and Knox, D. (2015), 'Prosthesis design and placement in reverse total shoulder arthroplasty', *Journal of Orthopaedic Surgery and Research*

- 10(101), 1–9.
- Adams, P. N., Laughlin, P. J., Monkman, A. P. and Bernhoeft, N. (1994), 'A further step towards stable organic metals. Oriented films of polyaniline with high electrical conductivity and anisotropy', *Solid State Communications* **91**(11), 875–878.
- Bae, B., Flachsbarth, B. R., Park, K. and Shannon, M. a. (2004), 'Design optimization of a piezoresistive pressure sensor considering the output signal-to-noise ratio', *Journal of Micromechanics and Microengineering* **14**(12), 1597–1607.
- Bao, Z. X., Colon, F., Pinto, N. J. and Liu, C. X. (1998), 'Pressure dependence of the resistance in polyaniline and poly(o-toluidine) at room temperature', *Synthetic Metals* **94**(2), 211–213.
- Barra, G. M. O., Matins, R. R., Kafer, K. A., Paniago, R., Vasques, C. T. and Pires, A. T. N. (2008), 'Thermoplastic elastomer/polyaniline blends: Evaluation of mechanical and electromechanical properties', *Polymer Testing* **27**(7), 886–892.
- Bergmann, G., Graichen, F., Bender, a., Käab, M., Rohlmann, a. and Westerhoff, P. (2007), 'In vivo glenohumeral contact forces-Measurements in the first patient 7 months postoperatively', *Journal of Biomechanics* **40**(10), 2139–2149.
- Berhouet, J., Garaud, P. and Favard, L. (2014), 'Evaluation of the role of glenosphere design and humeral component retroversion in avoiding scapular notching during reverse shoulder arthroplasty', *Journal of Shoulder and Elbow Surgery* **23**(2), 151–158.
- Bohsali, K. I. (2006), 'Complications of Total Shoulder Arthroplasty', *The Journal of Bone and Joint Surgery (American)* **88**, 2279.
- Castellanos-Ramos, J., Navas-González, R., Maclciór, H., Sikora, T., Ochoteco, E. and



- Vidal-Verdú, F. (2010), 'Tactile sensors based on conductive polymers', *Microsystem Technologies* **16**(5), 765–776.
- Cheung, E., Willis, M., Walker, M., Clark, R. and Frankle, M. a. (2011), 'Complications in reverse total shoulder arthroplasty.', *The Journal of the American Academy of Orthopaedic Surgeons* **19**(7), 439–449.
- Colby, S. L. and Ortman, J. M. (2015), 'Projections of the size and composition of the US population: 2014 to 2060', *Current Population Reports* pp. P25–1143.
- Costantini, O., Choi, D. S., Kontaxis, A. and Gulotta, L. V. (2015), 'The effects of progressive lateralization of the joint center of rotation of reverse total shoulder implants', *Journal of Shoulder and Elbow Surgery* **24**(7), 1120–1128.
- Del Castillo-Castro, T., Castillo-Ortega, M. M., Encinas, J. C., Herrera Franco, P. J. and Carrillo-Escalante, H. J. (2012), 'Piezo-resistance effect in composite based on cross-linked polydimethylsiloxane and polyaniline: Potential pressure sensor application', *Journal of Materials Science* **47**(4), 1794–1802.
- Della Pina, C., Zappa, E., Busca, G., Costa, P., Lanceros-Mendéz, S., Sironi, A. and Falletta, E. (2015), 'Towards "Green" Smart Materials for Force and Strain Sensors: The Case of Polyaniline', *Key Engineering Materials* **644**(July), 157–162.
- Della Pina, C., Zappa, E., Busca, G., Sironi, A. and Falletta, E. (2014), 'Electromechanical properties of polyanilines prepared by two different approaches and their applicability in force measurements', *Sensors and Actuators, B: Chemical* **201**, 395–401.
- D'Lima, D. D., Chen, P. C. and Colwell Jr., C. W. (2001), 'Polyethylene Contact Stresses, Articular Congruity and Knee Alignment', *Clinical Orthopaedics and Related Research* **392**(392), 232–238.

- D'Lima, D. D., Fregly, B. J., Patil, S., Steklov, N. and Colwell, C. W. (2012), 'Knee joint forces: prediction, measurement, and significance', *Proceedings of the Institution of Mechanical Engineers, Part H: Journal of Engineering in Medicine* **226**(2), 95–102.
- Falletta, E., Costa, P., Della Pina, C. and Lanceros-Mendez, S. (2014), 'Development of high sensitive polyaniline based piezoresistive films by conventional and green chemistry approaches', *Sensors and Actuators, A: Physical* **220**, 13–21.
- Gau, C., Ko, H. S. and Chen, H. T. (2009), 'Piezoresistive characteristics of MWNT nanocomposites and fabrication as a polymer pressure sensor.', *Nanotechnology* **20**(18), 185503.
- Giles, J. W., Langohr, G. D. G., Johnson, J. A. and Athwal, G. S. (2015), 'Implant Design Variations in Reverse Total Shoulder Arthroplasty Influence the Required Deltoid Force and Resultant Joint Load', *Clinical Orthopaedics and Related Research* **473**(11), 3615–3626.
- Grammont, P. M. and Baulot, E. (2011), 'The classic: Delta shoulder prosthesis for rotator cuff rupture. 1993.', *Clinical orthopaedics and related research* **469**(9), 2424.
- Guery, J., Favard, L., Sirveaux, F., Oudet, D., Mole, D. and Walch, G. (2006), 'Reverse total shoulder arthroplasty. Survivorship analysis of eighty replacements followed for five to ten years.', *The Journal of bone and joint surgery. American volume* **88**(8), 1742–1747.
- Holness, F. B. and Price, A. D. (2017), 'Design and fabrication of conductive polyaniline transducers via computer controlled direct ink writing', **10163**, 1–8.
- Hong, J., Pan, Z., Zhewang, Yao, M., Chen, J. and Zhang, Y. (2016), 'A large-strain weft-knitted sensor fabricated by conductive UHMWPE/PANI composite yarns', *Sensors and Actuators, A: Physical* **238**, 307–316.

- Hootman, J. M., Helmick, C. G., Barbour, K. E., Theis, K. A. and Boring, M. A. (2016), 'Updated Projected Prevalence of Self-Reported Doctor-Diagnosed Arthritis and Arthritis-Attributable Activity Limitation Among US Adults, 2015–2040', *Arthritis and Rheumatology* **68**(7), 1582–1587.
- Jung, Y., Lee, D. G., Park, J., Ko, H. and Lim, H. (2015), 'Piezoresistive tactile sensor discriminating multidirectional forces', *Sensors (Switzerland)* **15**(10), 25463–25473.
- Kang, J. H., Park, C., Scholl, J. A., Brazin, A. H., Holloway, N. M., High, J. W., Lowther, S. E. and Harrison, J. S. (2009), 'Piezoresistive characteristics of single wall carbon nanotube/polyimide nanocomposites', *Journal of Polymer Science B: Physics* **47**(10), 994–1003.
- Kim, S. H., Wise, B. L., Zhang, Y. and Szabo, R. M. (2011), 'Increasing incidence of shoulder arthroplasty in the United States.', *The Journal of bone and joint surgery. American volume* **93**(24), 2249–54.
- Kwon, Y. W., Forman, R. E., Walker, P. S. and Zuckerman, J. D. (2010), 'Analysis of Reverse Total Shoulder Joint Forces and Glenoid Fixation', *Bulletin of the NYU Hospital for Joint Diseases* **68**(4), 273–280.
- Langohr, G. D. G., Giles, J. W., Athwal, G. S. and Johnson, J. a. (2015), 'The effect of glenosphere diameter in reverse shoulder arthroplasty on muscle force, joint load, and range of motion', *Journal of Shoulder and Elbow Surgery* **24**(6), 972–979.
- Langohr, G. D. G., Willing, R., Medley, J. B., Athwal, G. S. and Johnson, J. A. (2016), 'Contact mechanics of reverse total shoulder arthroplasty during abduction: The effect of neck-shaft angle, humeral cup depth, and glenosphere diameter', *Journal of Shoulder and Elbow Surgery* **25**(4), 589–597.
- Lee, H. K., Chang, S. I. and Yoon, E. (2006), 'A flexible polymer tactile sensor: Fab-

- rication and modular expandability for large area deployment', *Journal of Microelectromechanical Systems* **15**(6), 1681–1686.
- Levigne, C., Garret, J., Boileau, P., Alami, G., Favard, L. and Walch, G. (2013), 'Scapular notching in reverse shoulder arthroplasty: Validation of a computer impingement model', *Bulletin of the NYU Hospital for Joint Diseases* **71**(4), 278–283.
- Martins, A., Quental, C., Folgado, J., Ambrósio, J., Monteiro, J. and Sarmiento, M. (2015), 'Computational reverse shoulder prosthesis model: Experimental data and verification', *Journal of Biomechanics* **48**(12), 3242–3251.
- Matsen, F. A., Clinton, J., Lynch, J., Bertelsen, A. and Richardson, M. L. (2008), 'Glenoid Component Failure in Total Shoulder Arthroplasty', *JBJS-A, The Journal of Bone and Joint Surgery* pp. 885–896.
- Mattioli-Belmonte, M., Giavaresi, G., Biagini, G., Virgili, L., Giacomini, M., Fini, M., Giantomassi, F., Natali, D., Torricelli, P. and Giardino, R. (2003), 'Tailoring biomaterial compatibility: in vivo tissue response versus in vitro cell behavior', *The International journal of artificial organs* **26**(12), 1077–1085.
- Nam, D., Kepler, C. K., Nho, S. J., Craig, E. V., Warren, R. F. and Wright, T. M. (2010), 'Observations on retrieved humeral polyethylene components from reverse total shoulder arthroplasty', *Journal of Shoulder and Elbow Surgery* **19**(7), 1003–1012.
- Nambiar, S. and Yeow, J. T. W. (2011), 'Conductive polymer-based sensors for biomedical applications', *Biosensors and Bioelectronics* **26**(5), 1825–1832.
- Pereira, J. N., Vieira, P., Ferreira, A., Paleo, A. J., Rocha, J. G. and Lanceros-Méndez, S. (2012), 'Piezoresistive effect in spin-coated polyaniline thin films', *Journal of Polymer Research* **19**(2).

- Quental, C., Folgado, J., Fernandes, P. R. and Monteiro, J. (2015), 'Computational analysis of polyethylene wear in anatomical and reverse shoulder prostheses', *Medical and Biological Engineering and Computing* **53**(2), 111–122.
- Razak, S. I. A., Dahli, F. N., Wahab, I. F., Abdul Kadir, M. R., Muhamad, I. I., Yusof, A. H. M. and Adeli, H. (2016), 'A Conductive polylactic acid/polyaniline porous scaffold via freeze extraction for potential biomedical applications', *Soft Materials* **14**(2), 78–86.
- Shtayermman, O. (2001), 'Design, simulation and fabrication of micromachined piezoresistive pressure sensors on flexible substrates', *The Journal of Real Estate Finance and Economics* **23**(2), 441–442.
- Smith, S., Li, B., Buniya, A., Lin, S. H., Scholes, S., Johnson, G. and Joyce, T. (2015), 'In vitro wear testing of a contemporary design of reverse shoulder prosthesis', *Journal of Biomechanics* **48**, BMD1500176.
- Tashjian, R. Z., Burks, R. T., Zhang, Y. and Henninger, H. B. (2015), 'Reverse total shoulder arthroplasty: a biomechanical evaluation of humeral and glenosphere hardware configuration', *Journal of Shoulder and Elbow Surgery* **24**(3), e68–e77.
- Terrier, A., Reist, A., Merlini, F. and Farron, A. (2008), 'Simulated joint and muscle forces in reversed and anatomic shoulder prostheses', *Bone & Joint Journal* **90-B**(6), 751–756.
- Zumstein, M. A., Pinedo, M., Old, J. and Boileau, P. (2011), 'Problems, complications, reoperations, and revisions in reverse total shoulder arthroplasty: A systematic review', *Journal of Shoulder and Elbow Surgery* **20**(1), 146–157.

# **Chapter 3**

## **Design and performance**

### **characterization of a distributed conductive polymer pressure sensor arrays**

The previous chapter established the unmet need to fabricate conductive polymer force sensor arrays. This chapter outlines the design considerations for the fabrication of these sensor arrays as the first step toward addressing this need. The 3D-printing, signal acquisition process, and calibration apparatus are also explained in detail.

#### **3.1 Design and fabrication**

Two approaches to fabricate the sensors were considered: capacitive and through-thickness (Kang et al., 2009). The small-scale dimensions of each sensor element combined with the current limitations of 3D-printers make it difficult to replicate each sensor. It is also not yet possible to print a dielectric over the PANI for the assembly

of a capacitive sensor. Due to these challenges and the additional complexity of signal conditioning in capacitive sensors, the through-thickness sensing mode was selected in which the loads were applied perpendicular to the surface of the sensing elements.

### 3.1.1 Substrate material selection

To fabricate the sensors, the initial idea was to produce a UHMWPE filament that could be 3D printed. However, it was observed that reforming UHMWPE through extrusion breaks the long chains, and as a result it could no longer be considered to have the same properties. In addition, due to its viscosity, UHMWPE is not melt-processable. To solve this inconvenience, Rocha et al. (2014) formulated a powder blend of Acrylonitrile butadiene styrene (ABS) with UHMWPE based on various mass ratios of ABS:UHMWPE:SEBS (90:10:10 and 75:25:10). In the end, they were unable to create a printable monofilament when the weight percent of UHMWPE was greater than 25% compared with the ABS base.

In this work, polyaniline was first embedded into Polylactic Acid (PLA), a polymeric substrate. However, the PLA was too brittle to resist the load application when applied to the whole sensor. The PLA was then swapped out for a thermoplastic elastomer (TPE) filament in the shore hardness 80A (filaments.ca, CA). Since the 3D printer that had been modified to print Polyaniline and PLA simultaneously was not suited to print the TPE, the first prototype was printed with another 3D printer where the PANI was injected into the substrate model using a syringe. To be able to print the substrate and PANI simultaneously, another flexible filament with a shore hardness of 95A, called Cheetah, was acquired (Ninjatek, USA).

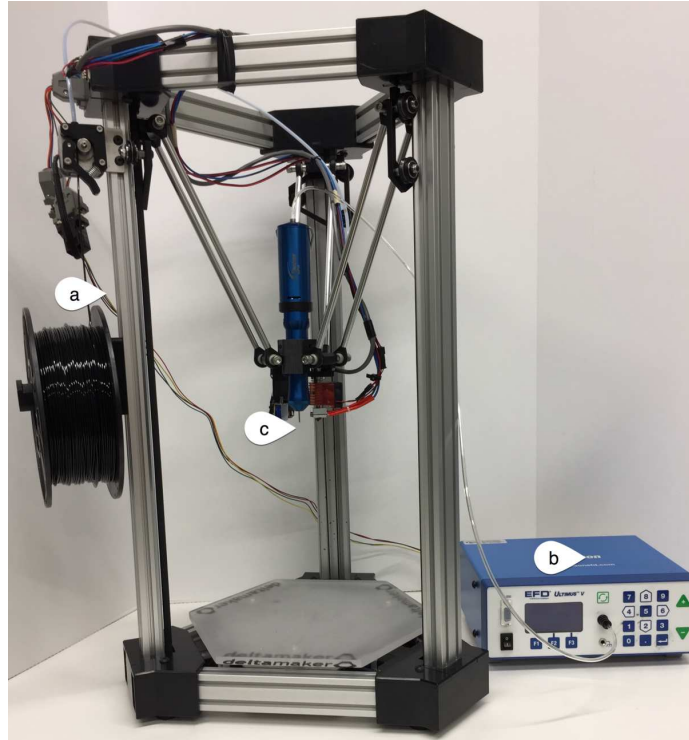


Figure 3.1: Modified fused filament fabrication delta robot (a) modified fused filament fabrication delta robot, (b) integrated paste extrusion system, (c) polymer paste cartridge, and (d) paste extrusion nozzle. (©Holness and Price (2016), included with permission.)

### 3.1.2 Sensor design

### 3.1.3 3D-printing

A specialized multi-material 3D printing technique, developed by Holness (2017), was utilized for the direct-ink writing process. This 3D printer uses a modified fused filament fabrication delta robot, equipped with an integrated polymer paste extruder, that allows it to print both materials simultaneously. The printer settings for each type of sensor are explained in more detail in section 4.1.2 for the flat sensor and in section 5.1.2 for the curved sensor.



### 3.1.4 Methods for wire connection

Two different materials were tested to determine which one would most efficiently connect the wires to the PANI elements: conductive carbon tape and silver epoxy. Silver epoxy was tested as suggested by Blythe (1984) as they indicate that the uncertain contact resistances at the contact point between the electrodes and the specimen can be reduced using silver epoxy. The precision by means of Root Mean Square Error (RMSE) was calculated for both methods of connection on the flat sensor following the protocols described in section 4.3.7, for each of the different load levels and connecting material. All the elements showed an average error ranging from  $RMSE_{avg,Element5} = 3.72\%$  to  $RMSE_{avg,Element2} = 5.38\%$  when silver epoxy connected the wires and the PANI, whereas these values ranged from  $RMSE_{avg,Element3} = 17.7\%$  to  $RMSE_{avg,Element7} = 74.94\%$  when carbon tape was used. The high RMSE values of carbon tape indicate an unstable connection between the wires and the PANI, therefore, silver epoxy was selected as the preferred method to connect the wires to the PANI in the sensors (MG Chemicals, Canada).

## 3.2 Signal acquisition and processing

A through-thickness sensing mode was employed to measure the changes in resistance in PANI, as explained in section 3.1. The voltages were then measured using a 32-input compact DAQ NI 9205 (National Instruments, USA) and an NI 9174 chassis (National Instruments, USA). Each sensing element was connected to an analog input to measure the voltages from the top surface of each PANI element, and another analog input was used to measure the applied voltage (nominal value of 2 V) in the whole circuit of the two-point probe used to measure the PANI resistance. This was done to compensate for any variation within the power supply. All of the elements were connected to the ground in the circuit and in the COM channel in the DAQ NI 9205.

A custom-made MATLAB (MathWorks, USA) software interface was developed to analyze the voltage signal and to calculate the resistance of PANI. A voltage-divider method was used to measure the resistivity according to the following equation:

$$R = \frac{R_S}{\left(\frac{V_{in}}{V_R}\right) - 1}, \quad (3.1)$$

where  $R$  is the variable PANI resistance measured,  $R_S$  is the shunt resistor of  $1000 \Omega \pm 1\%$  tolerance, in series with  $R$ ,  $V_{in}$  corresponds to the input voltage to the whole circuit, including  $R$  and  $R_S$ , and  $V_R$  is the voltage drop across  $R$ . The input voltage can be defined by the user, in this case,  $V_{in} = 2 \text{ V}$ . A filter was employed to introduce 60 Hz noise rejection while decreasing noise rejection at other frequencies and all negative resistivity was remapped to equal zero. Equation 3.1 was employed to measure  $R$  in each PANI element during each individual pressure load. Figure 3.2 depicts a schematic of the connection of a single PANI element for simplicity.

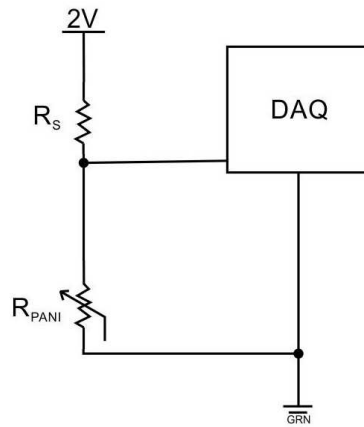


Figure 3.2: Schematic diagram showing the connection for one PANI element, consisting of PANI element ( $R_{PANI}$ ), Shunt Resistor ( $R_S$ ), and Data Acquisition System (DAQ) with a 2 V excitation.

A Matlab graphical user interface (GUI) was created to carry out the different experimental sets, where the user has the ability control the different parameters. The labels on the right of Figure 3.3 showcase the five different testing modes available for

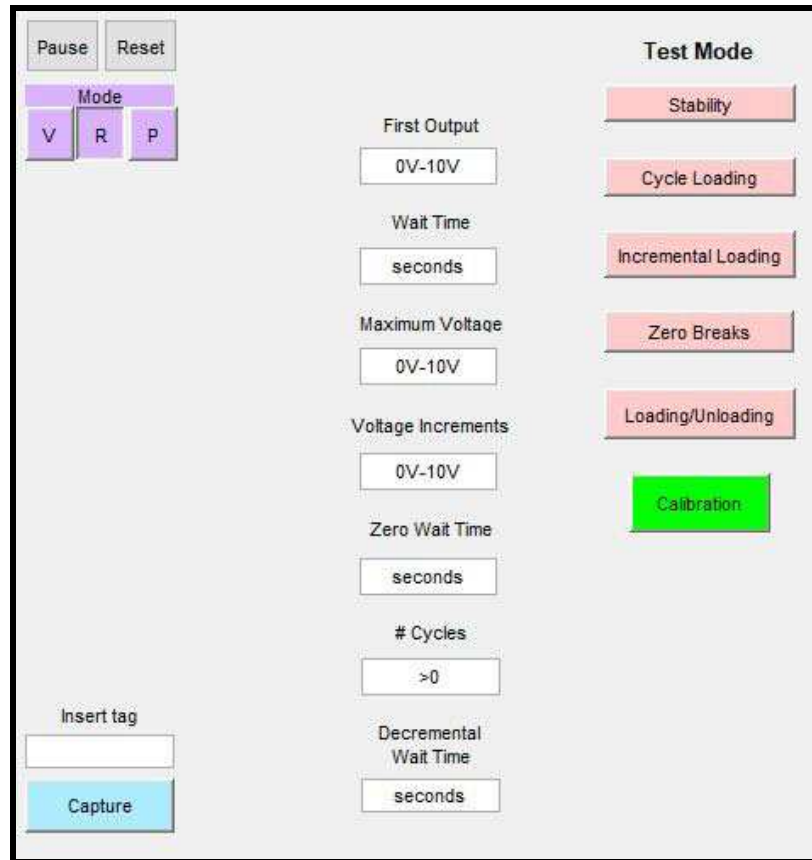


Figure 3.3: Test mode GUI showcasing the five different testing modes, as well as the parameters that can be input by the user.

characterization. These modes are explained in more detail in section 4.3. When the user selects the desired mode, only the parameters that can be changed in the current mode will appear.

During calibration, the software acquires a range of the resistance values, and applies linear curve fits to each grouping of data sets (there is one set for each polyaniline element: nine sets for the flat sensor and thirteen for the curve one). To enable the use of the elements as sensors, a GUI was created. This GUI allows the software to access the calibration data to give real-time feed-back to the user and plot the pressure matrix when its value is unknown. Figure 3.4 shows the GUI created for the flat sensor, while the GUI for the implemented joint replacement prosthetic can be found in section 5.4, Figure 5.13.

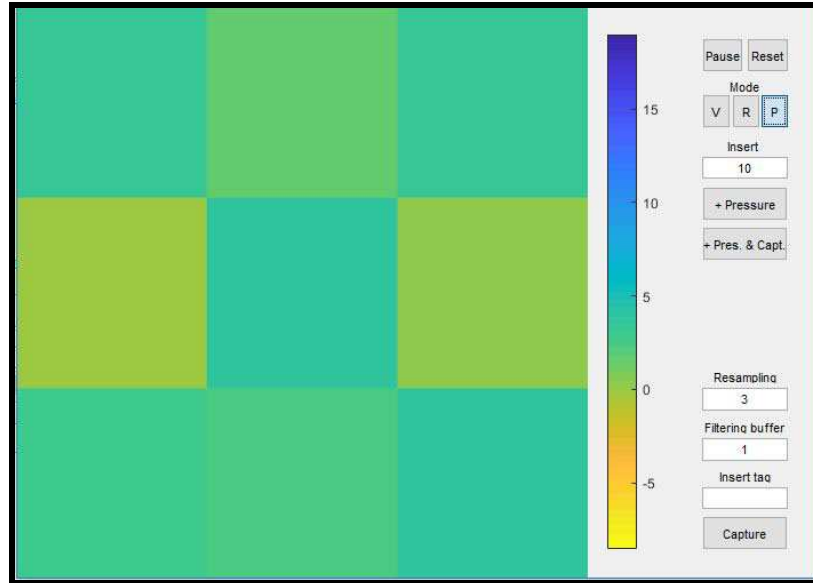


Figure 3.4: Flat sensor mode GUI showcasing the nine sensing elements (each coloured square).

### 3.2.1 Temperature compensation

This sensor is designed for the eventual use in cadaveric research that uses fresh frozen human cadaveric anatomy. Before they can be used, these specimens are thawed to a temperature between  $19\text{ }^{\circ}\text{C}$  to  $25\text{ }^{\circ}\text{C}$ , which corresponds to  $292.15\text{ K}$  to  $298.15\text{ K}$ . In their study of the relationship between temperature and the conductivity of PANI, Long et al. (2004) formulated an expression that models the temperature dependence of the resistivity of PANI-camphor sulfonic acid (PANI-CSA)/PANI-dodecylbenzene sulfonic acid (PANI-DBSA) blends. This expression can be used in the software to compensate for the resistivity change due to the change in temperature. However, the composition of polyaniline investigated by this group (90% PANI-DBSA/10% PANI-CSA) is not the same as the composition used in this study. Experimental results obtained by Long et al. (2004) for 80% PANI-DBSA and 90% PANI-DBSA, suggest that the behaviour of the dodecylbenzene sulfonic acid doped polyaniline (PANI-DBSA) is linear in the temperature range of interest and therefore its variation is negligible for this application.

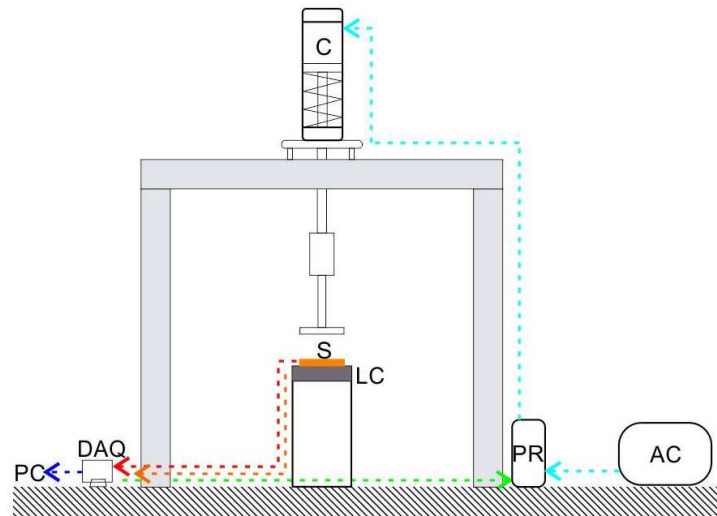


Figure 3.5: Calibration apparatus consisting of Air Cylinder (C), Pressure Regulator (PR), Air Compressor (AC), Data Acquisition System (DAQ), Load Cell (LC), Personal Computer (PC). A Sensor (S) is illustrated to demonstrate the placement at the time of characterization.

### 3.3 Calibration apparatus

As the ultimate goal was to develop a curved sensor, a calibration apparatus was specially designed to apply individual loads on each of the PANI elements to calibrate the curved sensor. This specially designed calibration apparatus, as depicted in Figure 3.5, consists of an air cylinder (Bimba, USA) in which the air flow is controlled by a QPV1 electronic pressure regulator (Equilibar, USA) driven by a NI 9263 (National Instruments, USA) on a NI 9174 chassis (National Instruments, USA). The applied load was corroborated by a LCAE 35KG load cell (Omega, USA), the electronic pressure regulator was driven by a NI 9263 (National Instruments, USA) on an NI 9174 chassis (National Instruments, USA), the pressure regulator was driven by a Data acquisition system NI 9263, and the load cell's output was measured using a DAQ 9205.

For the planar prototype, a flat surface of  $30 \text{ mm} \times 30 \text{ mm}$  was used to apply consistent pressure to the sensor, shown in Figure 3.6. To calibrate the curved sensor, and to apply a normal force to each of the PANI elements, a tilting device placed each PANI

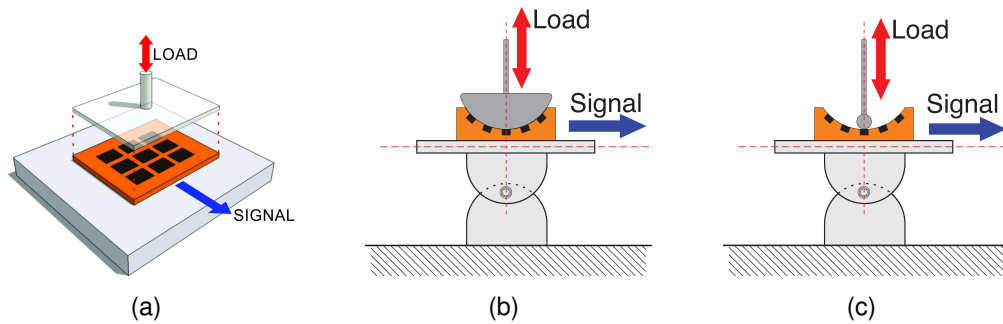


Figure 3.6: Schematic of the sensor configuration for piezoresistive characterization (a) Flat Array Characterization, (b) Curve Array Characterization, and (c) Curve Individual Characterization.

element under the calibration apparatus, and then the individual calibration was carried out with a rounded 12 mm point, shown in section 5.2 (Figure 3.6). The main source of error encountered with this calibration system is attributed to the electronic pressure regulator, which is rated for  $\pm 0.5\%$  full-scale accuracy.

### 3.4 Chapter summary

This chapter outlined the design features considered for the manufacturing of these polymeric sensors. A theoretical analysis was used to determine the materials that should be used for the fabrication of the supporting element, for the connection of the sensor elements with the wires, as well as for the temperature compensation. The 3D-printing technique was also presented. The signal acquisition and processing of the obtained data was explained in detail, and examples of the custom GUI created for this study were presented. Finally, the specially designed calibration apparatus was described in detail.

## List of references

- Blythe, A. (1984), 'Electrical resistivity measurements of polymer materials', *Polymer Testing* **4**(2-4), 195–209.
- Holness, F. B. (2017), Additive manufacturing process of 3D polyaniline transducers via direct ink writing, Master's thesis, The University of Western Ontario.
- Holness, F. B. and Price, A. D. (2016), Robotic extrusion processes for direct ink writing of 3D conductive polyaniline structures, in Y. Bar-Cohen and F. Vidal, eds, 'Electroactive Polymer Actuators and Devices (EAPAD) 2016', Vol. 9798 of *SPIE Smart Structures and Materials + Nondestructive Evaluation and Health Monitoring*, SPIE, Bellingham, WA, pp. 97981G–1 – 97981G–8.
- Kang, J. H., Park, C., Scholl, J. A., Brazin, A. H., Holloway, N. M., High, J. W., Lowther, S. E. and Harrison, J. S. (2009), 'Piezoresistive characteristics of single wall carbon nanotube/polyimide nanocomposites', *Journal of Polymer Science B: Physics* **47**(10), 994–1003.
- Long, Y., Chen, Z., Wang, N., Li, J. and Wan, M. (2004), 'Electronic transport in PANI-CSA/PANI-DBSA polyblends', *Physica B: Condensed Matter* **344**(1-4), 82–87.
- Rocha, C. R., Perez, A. R. T. and Roberson, D. A. (2014), 'Novel ABS-based binary and ternary polymer blends for material extrusion 3D printing', *J. Mater. Res.* **29**(17), 1859–1866.

# Chapter 4

## Characterization of a distributed planar conductive polymer pressure sensor array <sup>†</sup>

This chapter describes the characterization of polyaniline as a sensing element, for the internal forces in joint implants. In this regard, a 3D-printed flat sensor was created using in a  $3 \times 3$  array of PANI rectangular prisms embedded in a flexible polymeric substrate, to then be extended to an implant's geometry as conceptualized in Figure 4.1.

### 4.1 Design and fabrication

#### 4.1.1 Sensor design

The piezoresistive property of PANI was harnessed as a pressure sensor for the 3D-printed part. The sensor, a  $3 \times 3$  array of polyaniline rectangular prisms embedded

---

<sup>†</sup>Adapted from "Assessment of Embedded Conjugated Polymer Sensor Arrays for Potential Load Transmission Measurement in Orthopaedic Implants," by **Micolini, C**, Holness, FC, Johnson JA, & Price, AD, *Sensors* 2017, **17**(12), p. 2767. CC BY 4.0. Available from: MDPI [doi: [10.3390/s17122768](https://doi.org/10.3390/s17122768)]



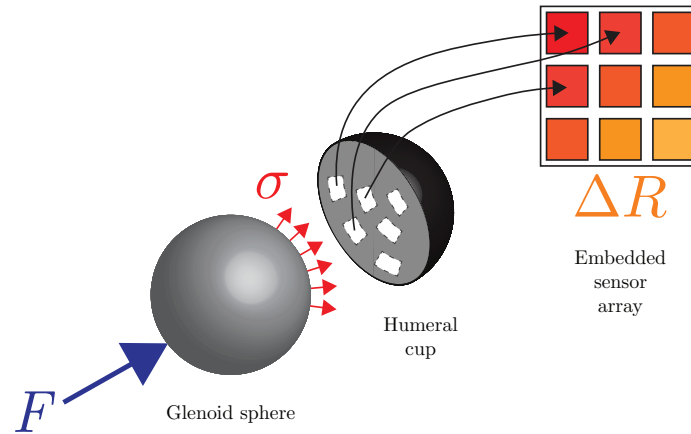


Figure 4.1: Conceptual representation of an orthopaedic implant with an embedded smart-polymer sensor network.

in a flexible polymeric substrate, was modeled using SolidWorks 2016 R2016a (Dassault systemes, France). This pattern was created to demonstrate that it is possible to distinguish between different pressures in various areas, monitoring across the whole surface. The dimensions of the sensor are  $30 \text{ mm} \times 30 \text{ mm} \times 2.5 \text{ mm}$ . These dimensions are approximately the same area of the spherical cap used on a humeral cup of an RTSA, which corresponds to  $1272.27 \text{ mm}^2$  for the design presented in section 5.1.1. The size of each polyaniline rectangular prism, measuring  $3.5 \text{ mm} \times 3.5 \text{ mm} \times 2.5 \text{ mm}$ , was chosen to facilitate their 3D printing simultaneously with the TPE (see Figure 4.2). There was a gap of  $0.5 \text{ mm}$  left between the PANI and the TPE to allow for deformation and to avoid the overlap of the two materials during the printing of the PANI elements. The distance between the centers of each element was set to  $9 \text{ mm}$ .

### 4.1.2 3D-printing

The flexible polymeric substrate was 3D printed using:  $1.75 \text{ mm}$  Cheetah filament, a thermoplastic elastomer (TPE) filament that has a shore hardness of 95A (Ninjatek, USA) and PANI doped by the use of dodecyl benzene sulfonic acid (DBSA), that was prepared according to the protocols described by Holness and Price (2016). This model

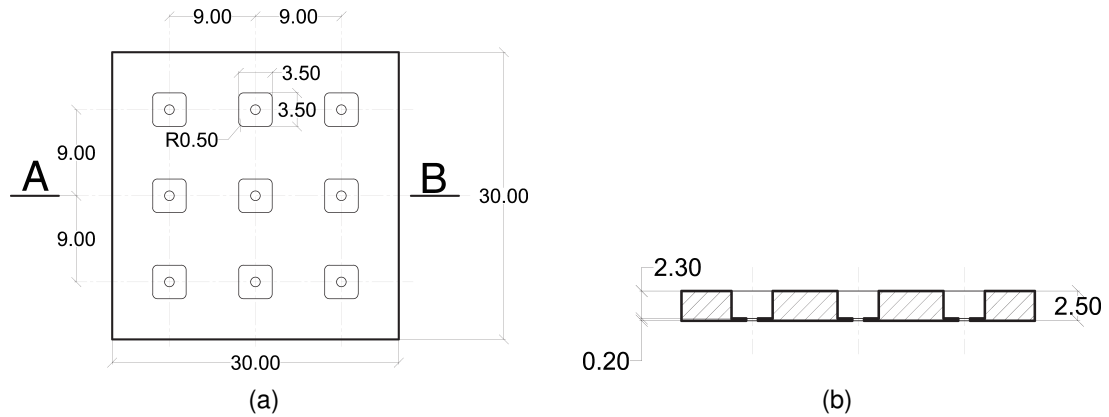


Figure 4.2: CAD illustration of the design for the flat sensor, displaying: (a) Top View, (b) Cross section A-B.

was printed using a specialized multi-material 3D printing technique that was developed at Western's Organic Mechatronics and Smart Materials Laboratory. This technique is used for direct-ink writing processes that use a modified fused filament fabrication delta robot equipped with an integrated polymer paste extruder, as discussed in section 3.1.3. Following the guidelines for this technique, the PANI was dispensed in a rectilinear ( $\pm 45^\circ$ ) fill pattern (without a perimeter wall) using a 22 Gauge stainless steel tip (Nordson, USA). The flexible polymeric substrate has a removable base where the PANI is injected to affix the part onto the build plate during printing. There are also 3 solid layers on the bottom and top and 2 perimeter outlines. The part was printed at  $230^\circ\text{C}$  with a rectilinear ( $\pm 45^\circ$ ) infill configured to 15% to ensure that the TPE deformed with and still enclosed the PANI. Figure 4.3 shows a screen capture of the printing pattern, showing print lines and fill pattern generated by Simplify3D (Simplify3D, USA). Figure 4.4 illustrates the fabricated sensor consisting of a  $3 \times 3$  array of polyaniline rectangular prisms, each one considered as an *element*, embedded in a flexible polymeric substrate.

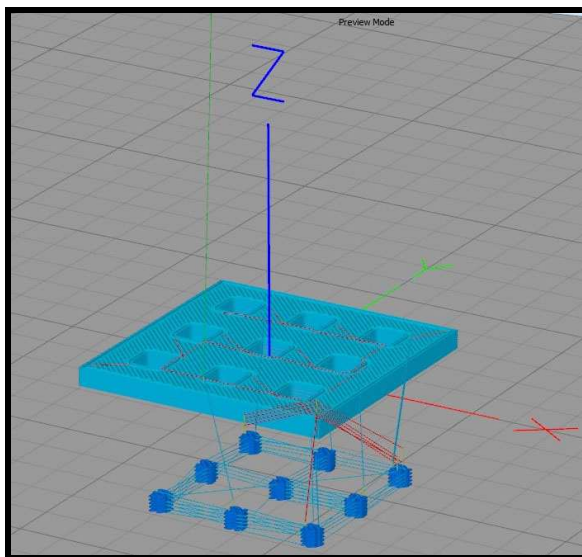


Figure 4.3: Screen capture generated by Simplify3D of the printing pattern, showing print lines and fill pattern.

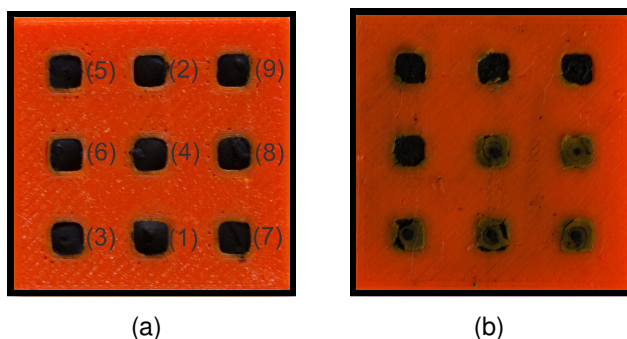


Figure 4.4: 3D-printed sensor array without the wires **(a)** Front view, with elements array description and **(b)** Back View - bottom elements showing the base used to prevent the injected PANI to slide onto the build plate of the printer.

### 4.1.3 Thermal treating and wiring

While preparing the PANI-DBSA paste, the mix was pre-thermal doped for 3.5 min over a 100 °C hot plate. After the 3D printing, the unwired-sensor was weighed before the post-thermal treatment of 165 °C for 5 min on a covered hot plate (Del Castillo-Castro et al., 2012). Its initial weight was 1.8980 g and when it was weighed again immediately after the treatment, the final weight was 1.8575 g. The 0.0405 g difference is due to the loss of moisture through evaporation (Barra et al., 2008). After each PANI element was treated with a thermal doping, it then needed to be wired. As discussed in section 3.1.4,

silver epoxy (MG Chemicals, Canada) was used as a means of connecting the PANI to the wires.

## 4.2 Calibration apparatus

Compression tests were carried out at room temperature using the specially designed calibration apparatus described in section 3.3. A flat surface measuring 30 mm  $\times$  30 mm was used to apply consistent pressure to the sensor. The electronic pressure regulator was driven by a NI 9263 (National Instruments, USA) on an NI 9174 chassis (National Instruments, USA), and the applied load was corroborated by a LCAE 35KG load cell (Omega, USA). The pressure regulator was driven by an NI 9263 data acquisition system, and the output of the load cell was measured using a DAQ 9205. Figure 4.5 illustrates the sensor setup during all tests of piezoresistive characterization.

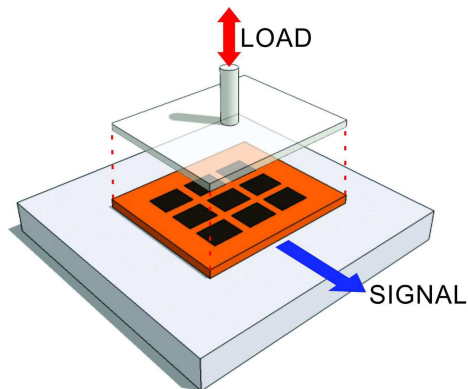


Figure 4.5: Schematic of the sensor's setup for piezoresistive characterization.

## 4.3 Performance characterization

After the sensor was printed, thermally treated, and wired, the sensor's piezoresistive characterization was undertaken, utilizing the specially designed calibration apparatus

previously described, to conduct a series of six separate tests. Equation 3.1 was used to measure  $R$  in each PANI element during each individual pressure load. To ensure a balanced distribution of the load steps in all test sets, the load values were chosen as incremental percentages of the input pressure supplied by the air compressor of the calibration apparatus (551.58 kPa). All tests were carried out at a nominal applied voltage of 2 V, as measured by the Data Acquisition (DAQ) system and used to calculate the resistance, to compensate for any variation of the power supply.

### 4.3.1 Stability

The resistance of the elements were first measured without an applied load, and then measured under a constant load for a given period of time. The resistance of the elements was measured without an applied load for the first 160 s, for a total of 12 measurements. Afterward, a 6.78 N load was applied and the elements were left to stabilize for 35 s, after that time the first measurement of the resistance under load was taken, with a total of 41 measurements under load taken in a 1966 s period.

### 4.3.2 Cyclic loading

Loading/unloading cycles of the elements were carried out, applying the same load in each cycle. Loaded measurements were taken using a 27.58 kPa input for the air cylinder, corresponding to a 5% input of the 551.58 kPa supplied by the air compressor of the calibration apparatus, which applies a total load of 6.78 N onto the sensor. The first measurement was taken without an applied load ( $R_0$ ), and then the sensor was loaded for 30 s, in order to allow the PANI to stabilize at the new load level of 8.5 N (Della Pina et al., 2014), subsequently the loaded measurement ( $R_{5\%}$ ) was taken. After this measurement was taken, the sensor was left unloaded for 30 s before a new loading/unloading cycle began. This process was repeated for 40 cycles, resulting in a

total of 80 resistance measurements.

Plots were obtained by introducing the following relationships:

$$Point_{0,n} = \frac{R_{0,n} - R_{0,n-1}}{R_{0,n-1}}, \quad (4.1)$$

$$Point_{5\%,n} = \frac{R_{5\%,n} - R_{0,n}}{R_{0,n}}, \quad (4.2)$$

where  $R_0$  corresponds to the value for the unloaded-resistance measured, and  $R_{5\%}$  corresponds to the value for the loaded-resistance measured.

### 4.3.3 Incremental continuous loading

An incremental loading from 0 N up to 50.84 N, with a loading step of 3.4 N was performed. After each incremental load was applied, the elements were left to stabilize for 60 s, then the measurements were taken and the load increased again, repeating the procedure. As the sensor response represents a first-order system, the stabilization period ensures consistency between measurements and aids in characterizing the response.

The fractional change in resistance ( $\Delta R/R_0$ ) was calculated.  $\Delta R$  is the difference between the resistance measured while the load is being applied and the resistance measured without the load over the sensor, and  $R_0$  is the resistance at no-load.

### 4.3.4 Incremental loading: zero breaks

An incremental loading from 20.34 N to 84.73 N, in 3.4 N steps was performed. After the load was applied, the elements were left to stabilize for 60 s before the loaded resistance values were measured. After taking these measurements, the load was removed and the elements were left unloaded for 60 s, before reloading the elements again with the increased load and repeating the measured procedure up to 84.73 N.

### 4.3.5 Loading/unloading cycle

A loading/unloading cycle carrying the load from 0 N – 50.84 N, in steps of 8.5 N was performed. Then the load was decremented in steps of 8.5 N, carrying the load from 50.84 N – 0 N. During the loading cycle, the elements were subjected to loading for 60 s before the resistance measurement was taken. After taking the measurement, the load was increased again. During the unloading cycle, the load was decremented, and the elements were subjected to the new load for 180 s before the new measurement was taken. The first measurement of the unloaded resistance was considered as 100% of the resistance value, and the rest of the resistances were calculated as a percentage of this one.

### 4.3.6 Repeatability

Three loading/unloading cycles were performed, letting the elements rest in between each cycle for a minimum of one hour. To better interpret the behavior of the curves, only data taken in the load cycles from 5% up to 30% of the 551.58 kPa input for the air cylinder are presented, as this range corresponds to the linear region of the data.

### 4.3.7 Precision

To calculate precision, the root mean square (RMS) of the error between the measurements taken in each one of the three loading/unloading cycles were compared to the average of all the measurements obtained from the cycles, using the following formula:

$$RMSE = \sqrt{\frac{1}{n} \sum_{i=1}^n \left( \frac{R_n - \bar{R}}{\bar{R}} \times 100\% \right)^2}. \quad (4.3)$$

## 4.4 Results

The aim of these tests was to assess the capability of the specialized multi-material 3D printing technique and the piezoresistive characteristics of PANI to manufacture embedded sensors for various applications, specifically for the analysis of joint loads in orthopaedic implants. To this end, the piezoresistive characteristics of the as-prepared polyaniline were analyzed. Linear fits were used on all incremental loading test sets as a linear response was expected for the change in resistance in relation to the applied load. After studying the results, non-linear factors have been observed and future studies are recommended to further investigate the source of these nonlinearities.

### 4.4.1 Stability

In this test set, Element #9 was discarded due to wire connection problems. Element #1 and Element #7 exhibit an abrupt drop in measurement for the same reason. In those cases when the sensor was unloaded, the wires did not make a good electrical contact, which resulted in high resistance values. Once the load was applied at 160 s, the load generated by the air cylinder ensured sufficient electrical contact. Figure 4.6 shows the measurements of Elements #2, #4, #5, #6 and #8. All show a stable response even without a load. This is done so there is no interference from the elements that showed bad connectivity.

The initial abrupt drop during the first seconds that the load was applied, can be attributed to the delay of the pneumatic piston to reach the desired load value. For all elements, the resistance values stabilize around the 7<sup>th</sup> minute of continuous load application. If the first loaded measurement of resistance for each element is considered to be 100% of the value for that series, it can be concluded that the percentage dropped to a maximum of 55.7% of its initial value for Element #1 and a minimum of 85.45% for Element #2, both are the final measurements taken, while the final values for the other



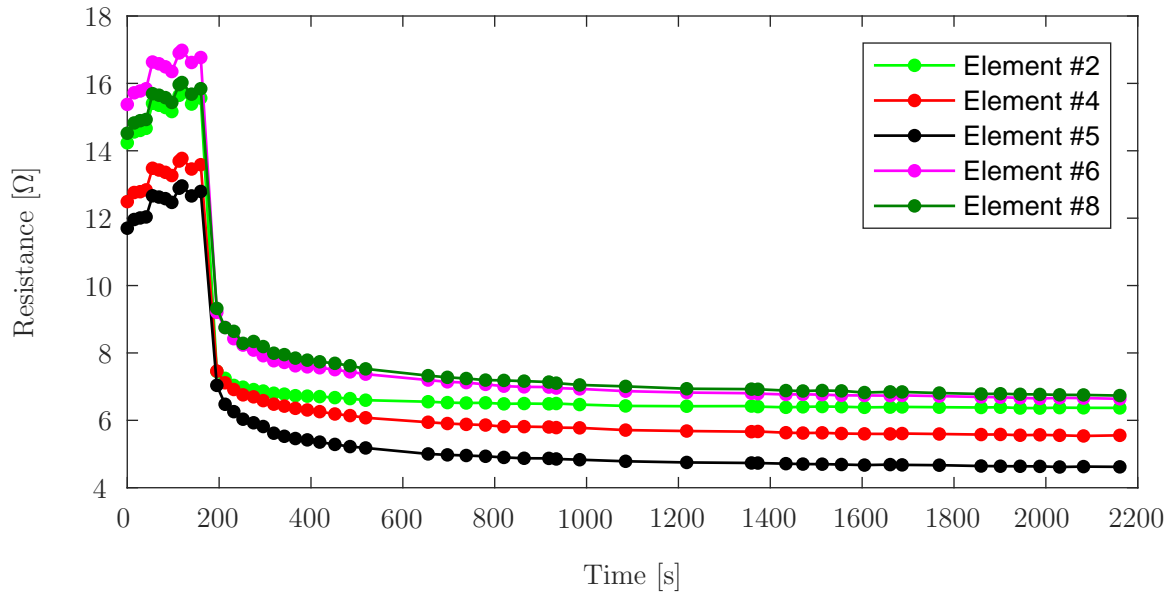


Figure 4.6: Change in resistance under no load and continuous load, for each PANI element.

elements fell in between this range.

#### 4.4.2 Cyclic loading

Two separate equations have been employed to visualize two trends: Equation (4.1) gives the difference between the measurements of unloaded-resistance versus the previous unloaded-resistance, plotted in Figure 4.7, while Equation (4.2) shows the difference between the loaded-resistance values and the unloaded-resistance values previous to the loading of the elements, plotted in Figure 4.8. The disturbance observed in cycles 37 and 38 for Element #5 are attributed to an overload of 170 N for this element after cycle 36.

#### 4.4.3 Incremental continuous loading

The value of the resistance at 3.4 N of applied pressure ( $R_0$ ) is considered to be 100%. All other values, at different applied pressures, are represented as a percentage of  $R_0$ . Figure 4.9 shows the change in resistance for each PANI element during incremental

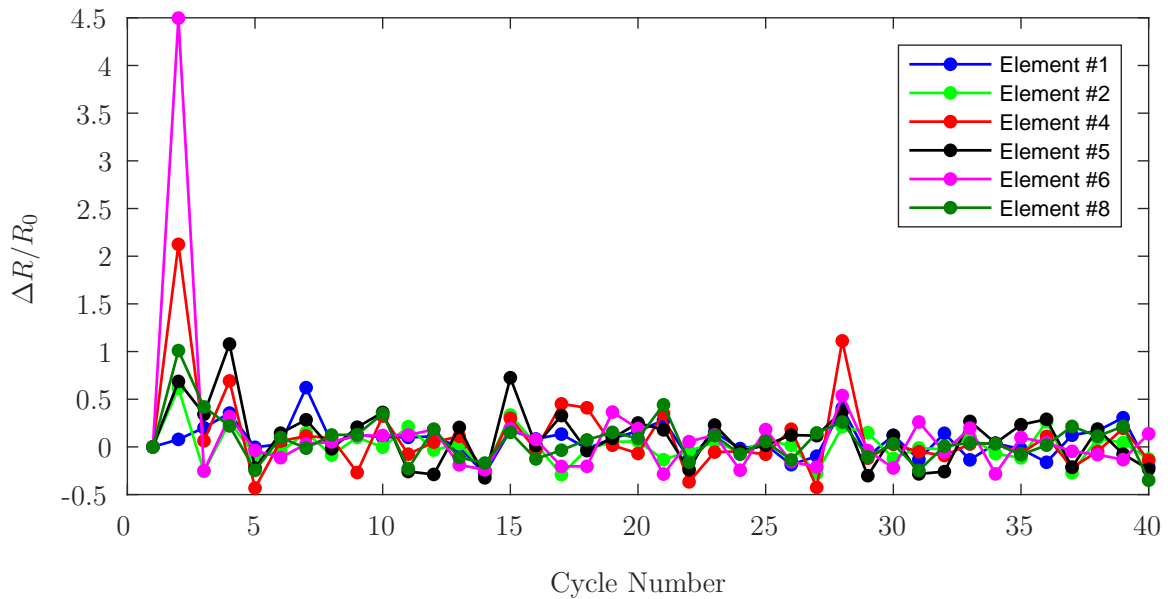


Figure 4.7: Fractional change in unloaded-resistance as a function of cyclic loading, for each PANI element.

continuous loading up to 30.5 N. After 30.5 N, the response of the elements tends to plateau, it also linear trendlines for each element, on which it can be seen how the trend lines are similar for all elements although the values are different.

#### 4.4.4 Incremental loading: zero breaks

Element #3 and Element #9 were excluded from the graph, as they either did not exhibit a significant change in resistance under load, or they exhibited erratic behavior attributed to poor electrical connectivity respectively.

#### 4.4.5 Loading/unloading cycle

Although all of the elements show similar curves, Element #4 is shown as a representative element to visualize the graph without interferences. Figure 4.11 shows the values measured for the relative change in resistance of Element #4 during the first loading/unloading cycle.

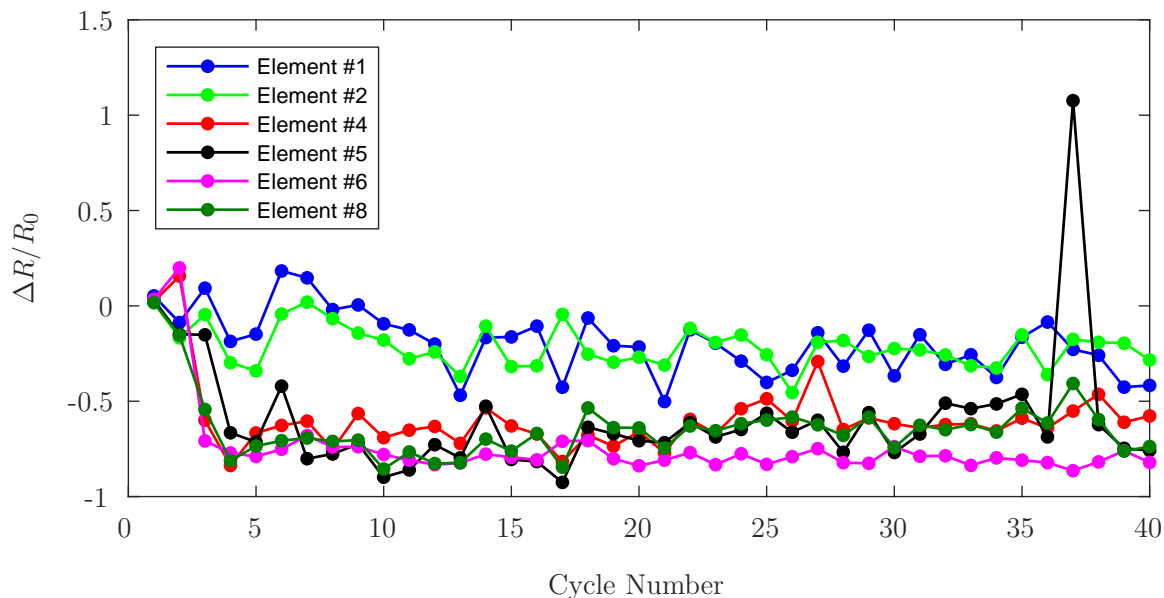


Figure 4.8: Fractional change in loaded-resistance as a function of cyclic loading, for each PANI element.

Table 4.1:  $R^2$  values for the linear fitting of sensor output.

	Element #1	Element #2	Element #4	Element #5	Element #6	Element #8
Series 1	0.81	0.85	0.76	0.79	0.78	0.81
Series 2	0.86	0.68	0.79	0.80	0.64	0.81
Series 3	0.84	0.68	0.78	0.78	0.71	0.82

#### 4.4.6 Repeatability

It can be observed in Figure 4.12 that the dynamics of the curve was repeated in the three cycles. Table 4.1 shows the  $R^2$  values used in the linear fitting, and only values for elements with good connectivity have been included.

#### 4.4.7 Precision

The maximum RMSE value of Element #6, was found to be  $RMSE_{Element6,16.95N} = 7.97\%$ , while the minimum value of Element #5, was  $RMSE_{Element5,8.47N} = 0.66\%$ . RMSE values for all other elements were in between, as shown in the next table. For all the different load levels, all the elements show an average error ranging from

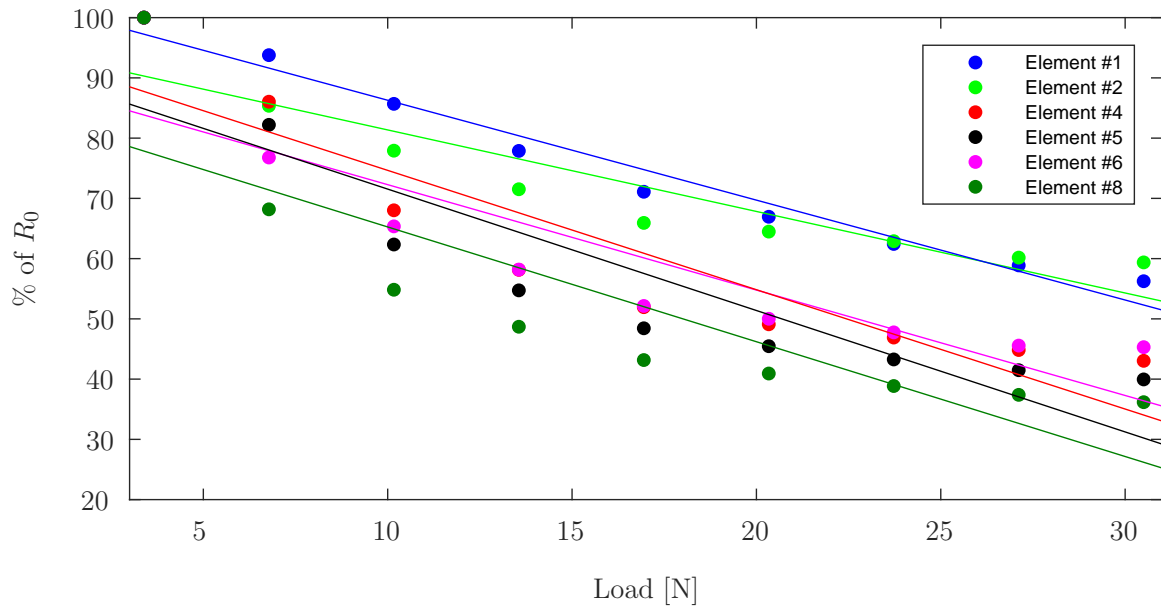


Figure 4.9: Linear fits for the change in resistance as a function of  $R_0$  during incremental loading, for each PANI element.

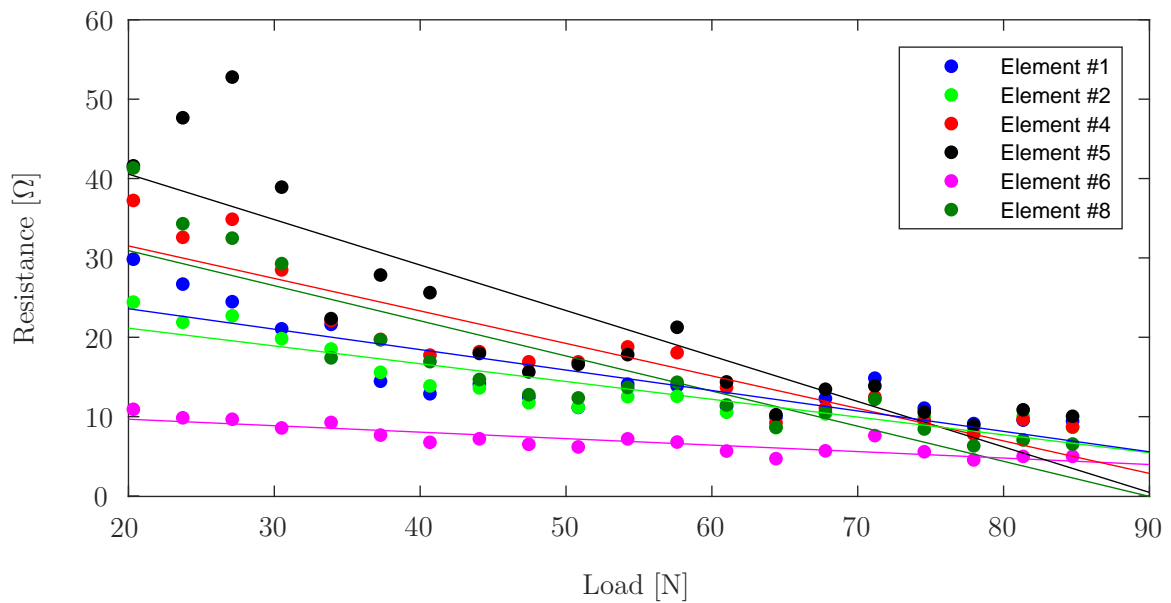


Figure 4.10: Linear fits for the change in resistance as a function of  $R_0$  during incremental loading-zero breaks, for each PANI element.

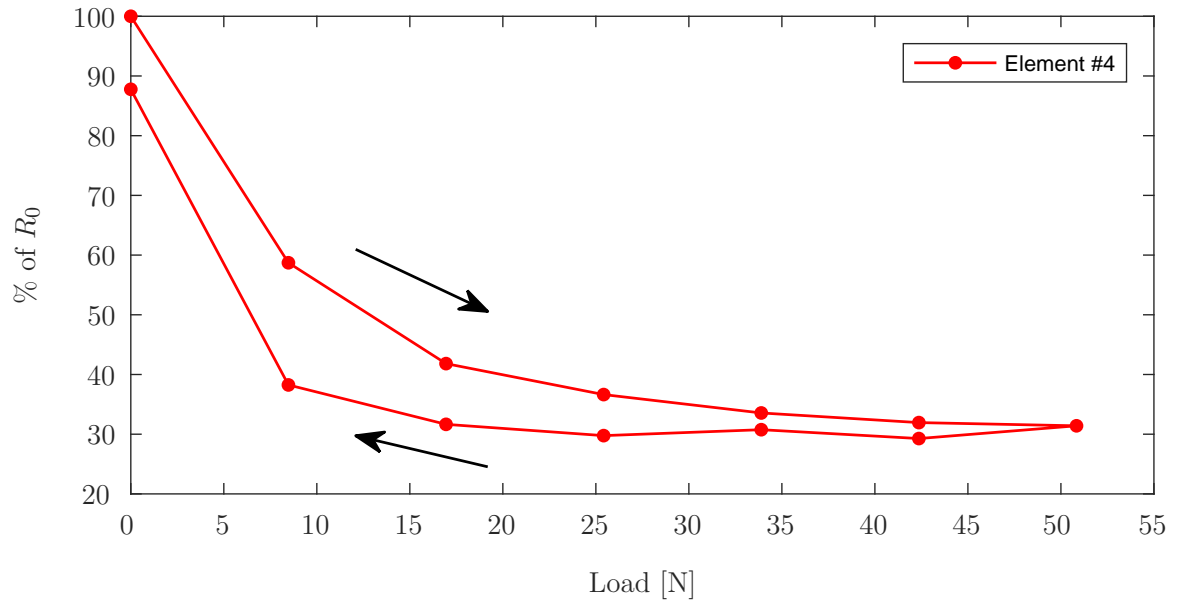


Figure 4.11: Relative change in resistance on Element #4 during the first loading/unloading cycle.

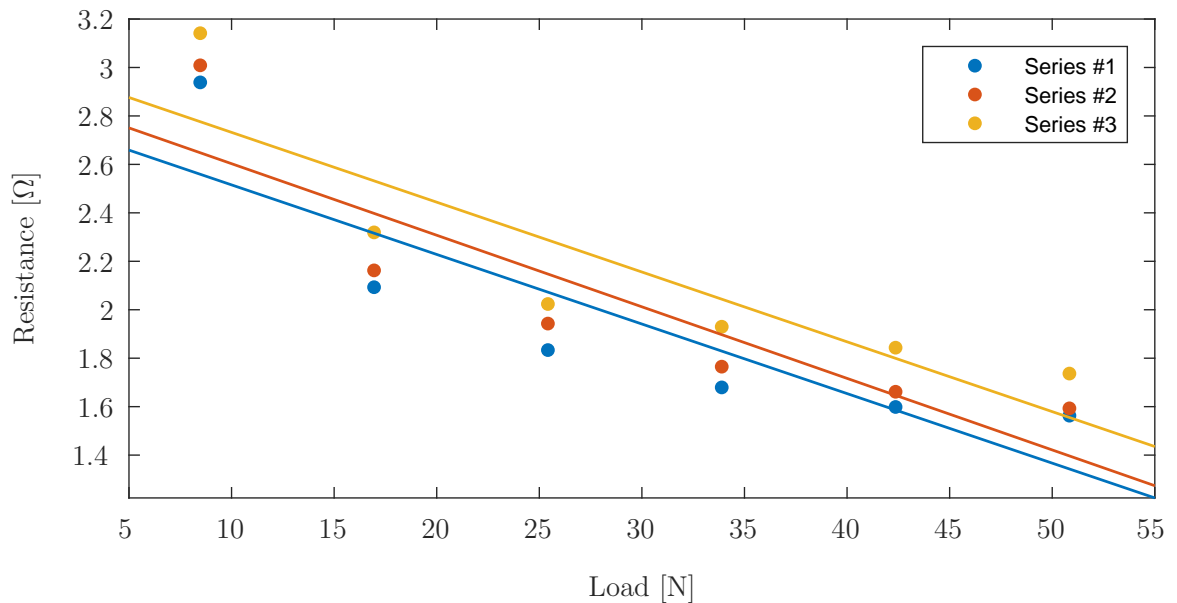


Figure 4.12: Change in resistance on Element #4 during the loading portion of the three repetitions of loading/unloading cycles as a function of load.

Table 4.2: Root Mean Square (RMS) of the error between the measurements taken in each one of the three loading/unloading cycles compared with respect to the average of the measurements obtained in all the cycles.

Load [N]	Element #1	Element #2	Element #4	Element #5	Element #6	Element #8
8.47	5.47%	7.19%	2.78%	0.66%	5.90%	4.88%
16.95	6.27%	5.19%	4.32%	1.99%	7.97%	5.00%
25.42	4.99%	4.49%	4.03%	2.86%	1.65%	4.41%
33.89	6.01%	5.49%	5.80%	5.24%	4.40%	3.35%
42.36	4.53%	2.71%	6.10%	6.34%	4.42%	2.98%
50.84	2.98%	7.28%	4.65%	5.21%	6.51%	4.47%

$$RMSE_{avg,Element5} = 3.72\% \text{ to } RMSE_{avg,Element2} = 5.38\%.$$

## 4.5 Discussion

In this chapter, a series of tests are presented to characterize and evaluate the potential for conductive polyaniline to be used for the 3D-printing technique to manufacture implant components embedded with smart-polymer sensors. The response of the PANI to a cyclical application of loads, its repeatable response to incremental compressive loading, the stability of its response to a continuous load, and the precision of these measurements, were used to corroborate the effectiveness of this material as a potential sensor. Due to current drawbacks associated with 3D printing, it is not possible to ensure an identical PANI deposition for each sensing element, simultaneously, the different amounts of silver epoxy used for the wire connections added to the lengths of these wires are translated in different resistances values for each sensing element. The wires were positioned to ensure similar heights among them, but for the aforementioned reasons, they may have had slight height differences that may have produced an uneven loading behavior. After all the test cycles were performed, and upon close inspection of the elements, the wires were not notably embedded in the PANI.

Following the cyclical application of loads, two separate equations were used to show two trends. Equation (4.1), used for Figure 4.7, shows that the difference between

the measurements of unloaded-resistance versus the previous unloaded-resistance ranges between  $\pm 50\%$ . This is consistent with the resistance returning to its pre-load value when no load is applied. This behavior is consistent with the observations reported by Barra et al. (2008), who attributes the re-organization of conduction pathways and elastic deformation of the matrix as the mechanisms for relative conductivity returning to its previous value upon unloading. Figure 4.8 shows the difference between the values of the loaded-resistance versus the unloaded-resistance previous to the loading of the elements.

During the cyclical loading, the measured resistance values for each element increased with each cycle in accordance with the observations made by Falletta et al. (2014), who suggest that this irregular behavior may be attributed to initial mechanical instabilities within the polymers. Both figures indicate that the fractional change in PANI's electrical resistance becomes more stable after 30 cycles.

It can be seen in Figure 4.9, showing linear trend lines for the data acquired during incremental continuous loading, that all elements have an initial nonlinear region, followed up by a linear region where PANI can perform as a sensing element. Both incremental continuous loading and incremental loading with zero breaks, verify a different behavior for Elements #3, #7, and #9 due to the faulty connection between the PANI and the wires, while the trend lines showed in Figure 4.9 are similar for the other elements although the values are different. This phenomenon can be confirmed since Elements #3 and #7 do not show notable changes in resistance measured under load or without load, and Element #9 shows erratic behavior corresponding to connectivity problems. Figure 4.12 shows the linear fit for the data acquired during the three cycles of piezoresistive characterization on Element #4, the resistance is plotted as a function of the applied load. Linear curve fits were applied to each set of measurements.  $R^2$  values were obtained as high as 0.8608 for the first cycle of Element #1, with an average value of 0.7803, and the lowest value found for Element #6 during the

second loading/unloading cycle with a value of 0.6447. With the application of increasing loads, the resistivity of PANI decreased linearly. Prior studies have observed that the reduced interchain separation coupled with the enhanced interchain charge transport, diminish the resistance of PANI while enduring a compressive load (Falletta et al., 2014; Barra et al., 2008; Bao et al., 1998). This demonstrates that PANI has a reliable response. However, the fragility of the connections between the PANI and the wires, that tend to get loose after a low number of loading cycles limit this reliability. Once the load was applied, the weight generated by the air cylinder was sufficient to ensure good electrical contact between the wires and the PANI elements. Since the developed PANI sensor arrays present a good linear relationship between the fractional changes in resistance during incrementally applied loads, together with a stable response, this specially developed multi-material additive manufacturing process for polyaniline is a potential candidate in the manufacturing of implant components embedded with smart-polymer sensors.

## **4.6 Chapter summary**

The design, fabrication, characterization, and signal acquisition and processing of a 3D-printed polymer sensor, with a  $3 \times 3$  conductive polyaniline structure array, was presented in this chapter. The characterization of the piezoresistive nature of the PANI elements embedded in the sensor and the calibration apparatus and technique were explained. The fractional change in resistance upon continuous loading, cyclical loading and unloading, and incremental loading, as well as the repeatability and precision of the loading/unloading cycles were discussed.



## List of references

- Bao, Z. X., Colon, F., Pinto, N. J. and Liu, C. X. (1998), 'Pressure dependence of the resistance in polyaniline and poly(o-toluidine) at room temperature', *Synthetic Metals* **94**(2), 211–213.
- Barra, G. M. O., Matins, R. R., Kafer, K. A., Paniago, R., Vasques, C. T. and Pires, A. T. N. (2008), 'Thermoplastic elastomer/polyaniline blends: Evaluation of mechanical and electromechanical properties', *Polymer Testing* **27**(7), 886–892.
- Del Castillo-Castro, T., Castillo-Ortega, M. M., Encinas, J. C., Herrera Franco, P. J. and Carrillo-Escalante, H. J. (2012), 'Piezo-resistance effect in composite based on cross-linked polydimethylsiloxane and polyaniline: Potential pressure sensor application', *Journal of Materials Science* **47**(4), 1794–1802.
- Della Pina, C., Zappa, E., Busca, G., Sironi, A. and Falletta, E. (2014), 'Electromechanical properties of polyanilines prepared by two different approaches and their applicability in force measurements', *Sensors and Actuators, B: Chemical* **201**, 395–401.
- Falletta, E., Costa, P., Della Pina, C. and Lanceros-Mendez, S. (2014), 'Development of high sensitive polyaniline based piezoresistive films by conventional and green chemistry approaches', *Sensors and Actuators, A: Physical* **220**, 13–21.
- Holness, F. B. and Price, A. D. (2016), Robotic extrusion processes for direct ink writing of 3D conductive polyaniline structures, in Y. Bar-Cohen and F. Vidal, eds, 'Electroactive Polymer Actuators and Devices (EAPAD) 2016', Vol. 9798 of *SPIE Smart Structures and Materials + Nondestructive Evaluation and Health Monitoring*, SPIE, Bellingham, WA, pp. 97981G–1 – 97981G–8.

# Chapter 5

## Application of smart-polymer sensor networks in an orthopaedic implant

This chapter presents the adjustments made to the flat polymeric sensor to facilitate use in a 3D joint replacement orthopaedic implant. An RTSA humeral cup model was chosen for the present assessment, as described in section 2.2.3. As presented in this chapter, a 3D-printed model of a 42 mm humeral cup was embedded with 13 conductive polyaniline prisms to act as the sensing elements. Alterations made to the calibration apparatus and the signal acquisition and processing method for the 3D sensor are also detailed in the following sections.

### 5.1 Design and fabrication

A 3D printed humeral cup was developed and instrumented with PANI-based embedded sensors, as shown in Figure 4.1. A greater quantity of sensing elements was used in the humeral cup sensor than previously used in the flat sensor. This was done to provide better distribution of forces across the PANI elements during joint loading. Due to the concave geometry of the humeral component of RTSA implants, modifications to

the calibration apparatus and load frame were required such that forces perpendicular to each PANI element could be applied for sensor calibration. In addition, adjustments were made to the custom MATLAB (MathWorks, USA) software interface to calibrate each PANI element individually, and not altogether as was previously done for the flat sensor.

### **5.1.1 Sensor design**

Following calibration of the flat sensor, the design was adapted to produce a 3D sensor based on the geometry of a 42 mm DePuy<sup>®</sup> humeral cup used in conventional RTSA procedures. The PANI sensing elements used on the curved surface of the humeral cup model were of the same size as those used previously on the flat sensor. The separation of the sensing elements was chosen so that each one covers the same surface of the humeral cup. Channels were made in the matrix, connecting the exterior of the sensor to the base of the PANI elements, to allow the wires to be threaded and connected to the sensors. In order to accommodate the channels for the wires, the height of the sides had to be raised, keeping the size of the cavity intact (see Figure 5.1).

Due to the current printing capabilities, the flexible polymer could not be printed onto the PANI. For this reason, the top surfaces of the sensing elements were left temporarily exposed. The exposed faces of the PANI elements allowed for the elements to be connected to ground wires before a fitted, 3D-printed, cover was adhered to embed the exposed PANI and complete the humeral cup geometry (see Figure 5.2).

### **5.1.2 3D-Printing and PANI deposition**

The curved base of the humeral cup model was printed and then the PANI infill was embedded manually. The desired connection points for the wires were on the bottom

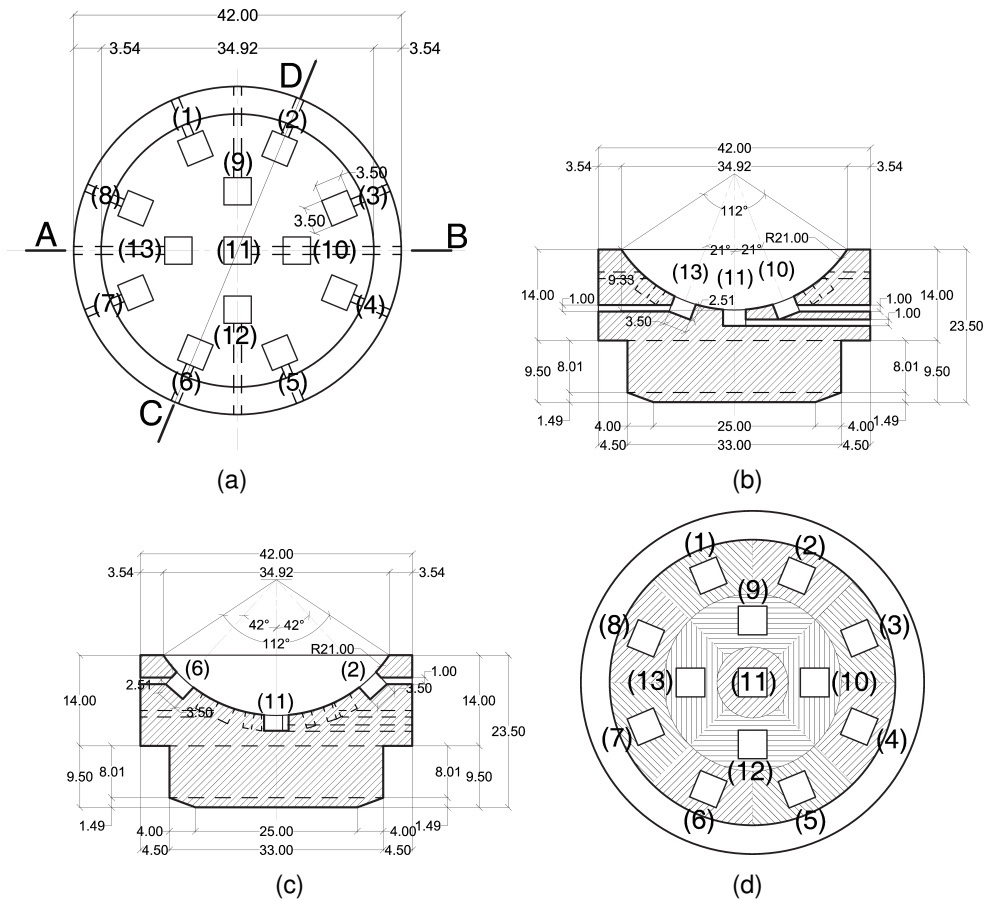


Figure 5.1: CAD illustration of the design for the humeral cup sensor, displaying: (a) Top View of the sensor base with numbered sensing elements, (b) Cross-section A-B, (c) Cross-section C-D, and (d) Surface covered by each sensing element.

of the sensor elements, and the 3D printing of the TPE resulted in some stringing effects across the voids. To avoid connection issues due to the stringing and facilitate wiring the bottom of the elements, it was decided to print the curved base first and then perform the PANI infill manually.

Both the curved base and the top cover for the humeral cup sensor were 3D-printed using 1.75 mm Cheetah filament, a thermoplastic elastomer (TPE) filament with a shore hardness of 95A (Ninjatek, USA). These parts were printed onto a heated bed set at 40 °C. The TPE filament was printed at 230 °C, using 3 solid layers on the bottom and top and 2 perimeter outlines. A rectilinear ( $\pm 45^\circ$ ) 15% infill pattern was

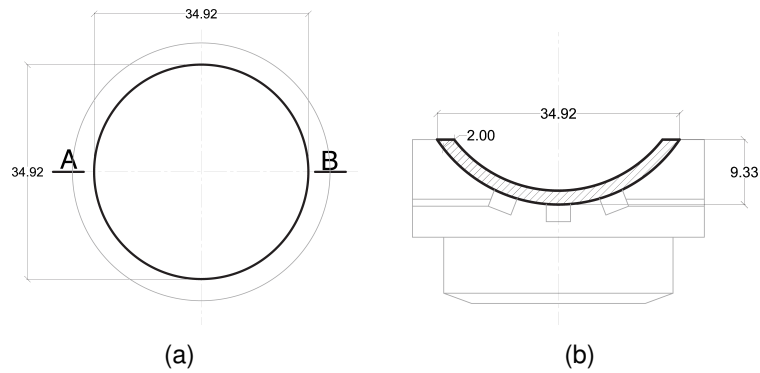


Figure 5.2: CAD illustration of the design for the humeral cup cover, displaying: (a) Top View and (b) Cross-section A-B.

used to ensure that the TPE was flexible enough to deform along with the PANI, while maintaining sufficient structure to enclose the PANI prisms.

The PANI was prepared according to the protocol described by Holness and Price (2016) and doped with dodecyl benzene sulfonic acid (DBSA). During the PANI-DBSA paste preparation, the mix was pre-thermal doped over a 100 °C hot plate, for 3.5 min total; in two intervals of 1 min and one interval of 1.5 min. The fabricated 3D sensor consisted of an array of polyaniline rectangular prisms, with a total of 13 sensing elements embedded in the TPE.

### 5.1.3 Wiring and thermal treating

As mentioned in section 5.1.1, the wires were threaded through the connecting channels as depicted in Figure 5.3. First, the wire was threaded and then the silver epoxy was deposited on top of it. Following the application of the silver epoxy, the PANI infill was manually applied into each cavity. The silver epoxy was also used to connect the wires to the ground. Once the elements were grounded, the top TPE cover was adhered to the base part using hot melt adhesive (HMA). After assembly, the sensor was thermally treated at 165 °C for 7 min on a covered hot plate.

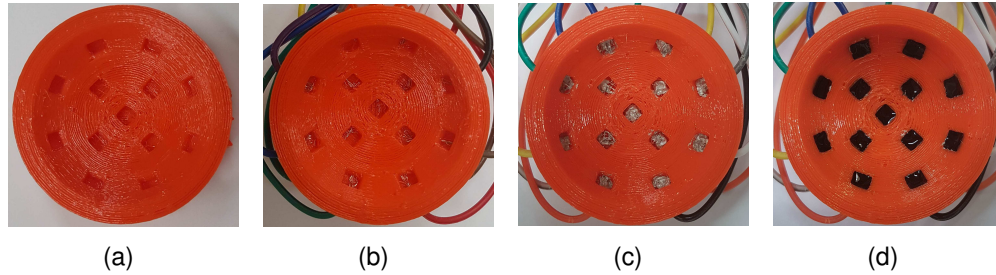


Figure 5.3: Wiring and PANI embedment procedure for the curved sensor. The steps include: (a) 3D-printing of the humeral cup base component, (b) Threading of wires through the connecting channels in the base, (c) Application of the silver epoxy, (d) PANI infill.

## 5.2 Adaptation of the calibration apparatus

Calibration of the 3D sensor required that the PANI elements each be calibrated individually. Unlike the flat sensor which allowed for joint calibration of all elements, individual calibration was required for the humeral cup sensor to ensure that each element was subjected to known compressive forces, acting perpendicular to the surface of the sensor. This required use of a loading setup capable of varying the angular position of the sensor in relation to the applied loading.

For the individual calibration, as shown in Figure 5.4, a metallic 8.3 mm diameter spherical head was used. To maintain a normal force during calibration of each PANI element, the sensor was secured to a tilting table. The position of the table could be adjusted to alter the angular position of the elements with respect to the direction of the applied force.

To orient the PANI elements normal to the applied force during calibration, the base of the system can be inclined to:  $0^\circ$  for the central element (#1),  $21^\circ$  for the middle elements (#9, #10, #12, #13), and  $42^\circ$  for the external elements (# 1–8). The sensor array was adjusted at the  $21^\circ$  and  $42^\circ$  angles to allow for the loading head to reach each element under evaluation in succession.

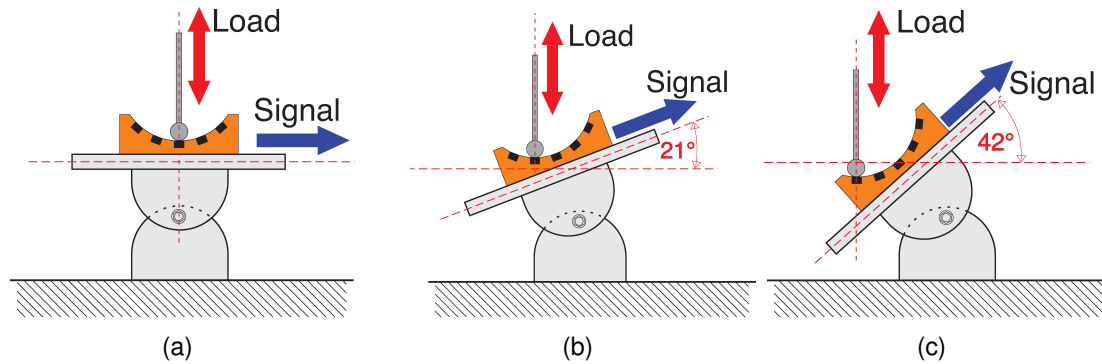


Figure 5.4: Illustration of the calibration apparatus for testing individual PANI elements in the curved sensor. The tilting table is shown, with the sensor adjusted to angles of: (a)  $0^\circ$ , (b)  $21^\circ$ , and (c)  $42^\circ$ .

### 5.3 Performance characterization

The through-thickness sensing mode was employed to measure the change in resistance of the PANI elements (Kang et al., 2009). Fourteen voltages were measured using a 32-input compact DAQ NI 9205 (National Instruments, USA) and an NI 9174 chassis (National Instruments, USA). Thirteen of the analog inputs were used to measure the voltages from the top surface of each PANI element, and one analog input was used to measure the applied voltage (nominal value of 2 V) in the whole circuit. The measuring circuit formed two-point probes to measure each PANI element's resistance. The connection between all PANI elements, on the underside of the sensor, was connected to the ground in the circuit and the COM channel in the DAQ. A custom-made MATLAB (MathWorks, USA) software interface was developed to analyze the voltage signal and to calculate the resistance of the PANI elements, as explained in section 3.2.

After the sensor was printed, thermally treated, and wired, testing of the 3D sensor and calibration of the individual PANI elements were carried out. Overall, a series of six tests was performed: cyclic loading test and stability test of the entire sensor, incremental loading tests of individual PANI elements, and three incremental loading tests of the entire sensor. The cyclic loading and stability tests used a glenoid sphere

from a commercially available RTSA implant to apply loads into the humeral cup sensor, as described in section 5.3.1 and section 5.3.2. The element calibrations were carried out using the adjusted apparatus, described in section 5.2. Equation 3.1 was used to measure  $R$  in each PANI element during all tests. All tests were carried out at an applied voltage of 2 V. The input voltage was monitored using the DAQ as well as the power supply. In case any variations occurred in the power supply, the input and output readings from the DAQ were used to calculate the resistance of the PANI elements during each test.

### 5.3.1 Cyclic loading

A commercially available glenoid sphere was used to apply loads to the whole sensor during cyclic loading and stability tests. Use of the glenoid sphere for loading the entire sensor at once resulted in some sensing elements being subjected to forces that did not act normal to the sensing surface. For this reason, the 3D sensor was tested under higher forces than those used with the flat sensor. Loading/unloading cycles were programmed to apply the same maximum load to the sensor during each cycle. Load application and measurements were taken using a 20% of the 551.58 kPa pressure supplied by the air compressor of the calibration apparatus, and results in a total applied load of 33.9 N. The first resistance measurements were taken with no applied load ( $R_0$ ). The sensor was then loaded to 33.9 N and held for 30 s in order to allow the PANI elements to stabilize at the new load level (Della Pina et al., 2014). At the end of the stabilization period, the loaded measurement ( $R_{20\%}$ ) was taken. After the resistance measurement was taken, the sensor was unloaded and left for 30 s before a new cycle began. This process was repeated for 40 cycles, providing a total of 198 resistance measurements.



Plots were obtained by introducing the following relations:

$$Point_{0,n} = \frac{R_{0,n} - R_{0,n-1}}{R_{0,n-1}}, \quad (5.1)$$

$$Point_{20\%,n} = \frac{R_{20\%,n} - R_{20\%,n-1}}{R_{20\%,n-1}}, \quad (5.2)$$

where  $R_0$  corresponds to the unloaded resistance, and  $R_{20\%}$  to the loaded resistance, measured during cycle  $n$ .

### 5.3.2 Stability

Similar to the cyclic testing in section 5.3.1, the commercial glenoid sphere was used to apply load to the whole sensor during this test. The resistance of the elements without any applied load was measured, then the element was loaded and held under constant load for an extended period of time. The unloaded resistance was measured for the first 180 s, providing a total of 34 measurements. Then, a 33.9 N load was applied and the elements were left to stabilize for 40 s before the first resistance measurements under load were taken. A total of 209 resistance measurements were taken from each loaded element over a 1950 s period. The following equation was used to calculate the change in the measured resistance, as a percentage of the first resistance  $R_{20\%,n_0}$  measured at 33.9 N of applied loading, which was taken as 100% of the element's resistance value:

$$Point_{20\%,n} = \frac{R_{20\%,n}}{R_{20\%,n_0}} \times 100\%. \quad (5.3)$$

### 5.3.3 Incremental continuous loading of individual elements

Incremental loading from 0 N up to 16.95 N was applied in steps of 1.7 N to each individual PANI element. The tilting table described in section 5.2 was used to adjust the angle of the sensor, relative to the load direction, so that each PANI element could

be loaded individually and normal to the sensing surface.

For the first applied load the elements were left to stabilize for 10 s before the first measurement was taken. For each incremental load applied, the elements were left to stabilize for 60 s taking measurements in intervals of 5 s. Then the load was increased again, to repeat the procedure. At the first load increment, the load was held for 10 s before the resistance measurement was taken. At each following increment, the load was applied then held for 60 s to allow the sensing elements to stabilize, while resistance measurements were taken at 5 s intervals. After the 60 s stabilization period, the load was increased to the next higher load increment. The load and measurement procedure was repeated for incremental loads up to 16.95 N.

The incremental loading sequence was applied to the sensor with the base inclined to various angles:  $0^\circ$  for the central element (#11),  $21^\circ$  for the middle elements (#9, #10, #12, #13), and  $42^\circ$  for the external elements (#1–8). This produced resistance results for the cases where each element of the array was subjected to loads normal to its sensing surface.

The fractional change in resistance ( $\Delta R/R_0$ ) was calculated for each element under incremental load changes.  $\Delta R$  is the difference between the loaded and unloaded resistance measurements, and  $R_0$  is the measured resistance when the element is under no load.

#### **5.3.4 Incremental continuous loading of the entire sensor at multiple angles**

Following the individual calibration tests, a similar, incremental load test was carried out on the entire sensor. Loads were applied using the glenoid sphere, ranging from 0 N up to 25.42 N, in 1.7 N steps. The glenoid sphere was used to apply forces to all elements at once. The test was carry out at  $0^\circ$ , but the tilting table can be adjusted to

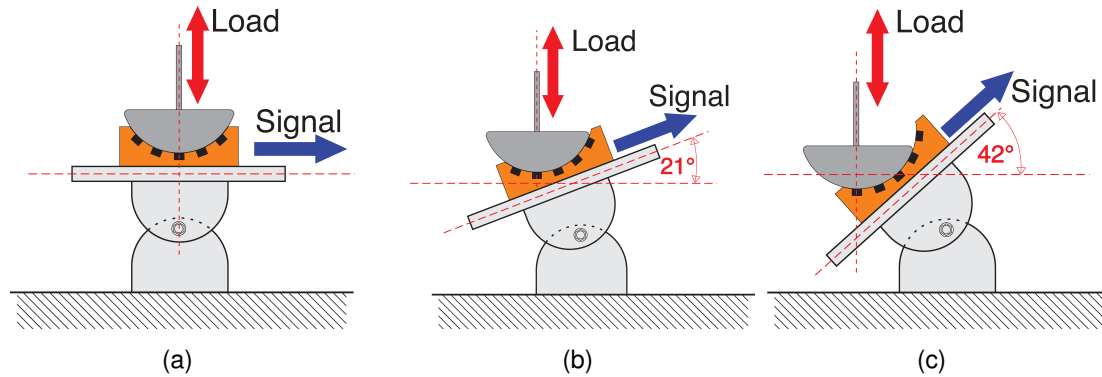


Figure 5.5: Illustration of the calibration apparatus for joint testing of the curved sensor. The tilting table is shown, with the sensor adjusted to angles of: (a)  $0^\circ$ , (b)  $21^\circ$ , and (c)  $42^\circ$ .

perform tests at different angles to assess the effects of loads applied to the humeral cup. Figure 5.5, shows the tilting table adjusted at  $0^\circ$ ,  $21^\circ$ , and at  $42^\circ$  angles as examples.

## 5.4 Signal acquisition and processing

A Matlab (MathWorks, USA) GUI was created to give real-time visualization of the results by plotting the load changes in the array of PANI elements. This GUI features a  $5 \times 5$  matrix, in which the thirteen PANI elements are represented by cells arranged in the same orientation as the elements in the humeral cup sensor, while the remaining twelve elements of the matrix are zeroed.

## 5.5 Results

The 3D sensor manufacturing technique presented herein can be widely applied to diverse prosthetic joint replacements. In this chapter the RTSA was chosen only as an example of an application of this technique. This particular sensor, which has a curved geometry, uses the humeral cup model as an example to demonstrate the design, fabri-

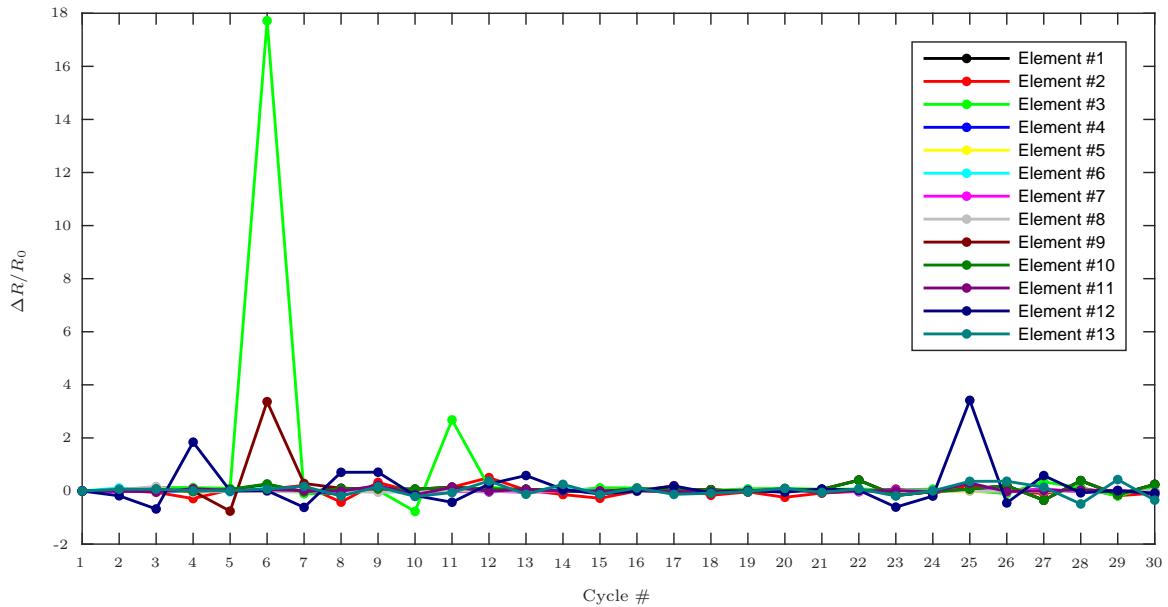


Figure 5.6: Fractional change in unloaded-resistance of PANI elements under cyclic loading. Resistance measurements were taken when the element was in an unloaded state.

cation, and calibration of a 3D sensor. Similar procedures can be carried out to develop sensors with different geometries for different types of implants. Analysis of the present 3D sensor test results is discussed in the following sections. Since the wire connections make it difficult to measure the sensor elements at zero load, the measurements taken with no load were excluded from the graphics in all test sets.

### 5.5.1 Cyclic loading

Two separate equations have been used to understand two trends in the results of the cyclic loading tests on the entire sensor. Equation (5.1) calculates the difference between the unloaded resistance measurement and the unloaded resistance measured in the previous cycle, plotted in Figure 5.6, while Equation (5.2) depicts the fractional change in the loaded resistance values between two consecutive loading cycles, plotted in Figure 5.7.

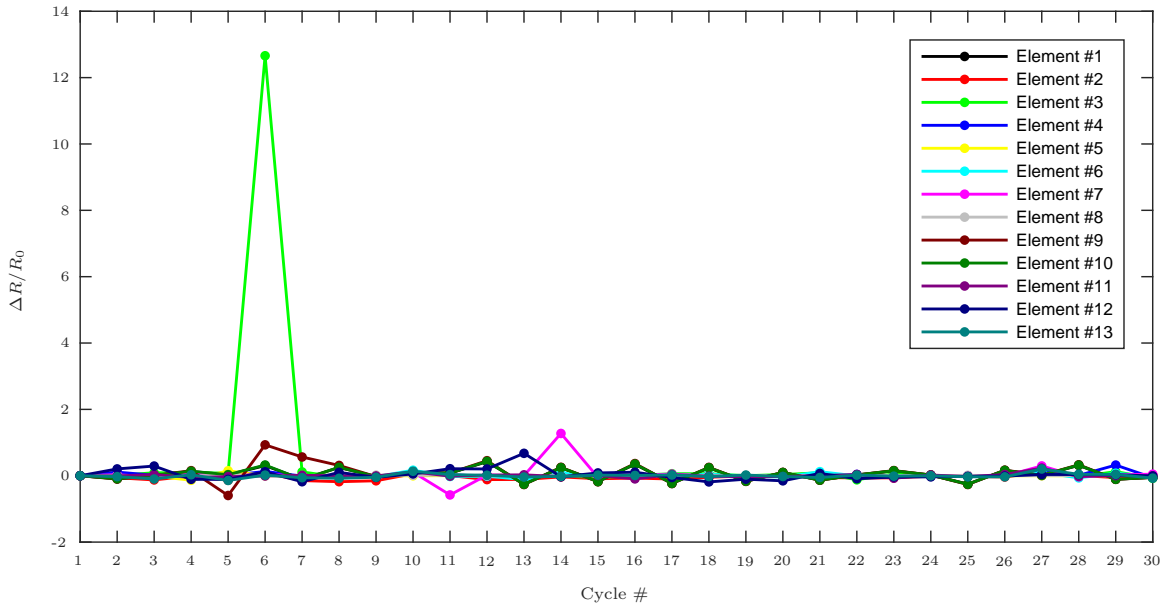


Figure 5.7: Fractional change in loaded-resistance of PANI elements under cyclic loading. Resistance measurements were taken under an applied load of 33.9 N

### 5.5.2 Stability

Equation (5.3) was used to calculate the change in the measured resistance for this test. Figure 5.8 shows the change in resistance during the continuous applied load of 33.9 N. Central element #11 does not present an apparent change in its resistance value. This can be attributed to the fact that this sensing element was located in line with a hole in the glenoid sphere which is used for the insertion of the screw that fixes the sphere to the bone. The hole prevented the surface of the sphere from transferring load into sensing element #11 during this test. The external element #5 also does not show an apparent change in its resistance value, making it evident that the glenoid sphere was not perfectly centered during the test.

### 5.5.3 Incremental continuous loading of individual elements

The measured resistance at 1.7 N of applied load is taken as ( $R_0$ ) and considered to be 100% of the PANI element's resistance. All other values, measured at different loads,

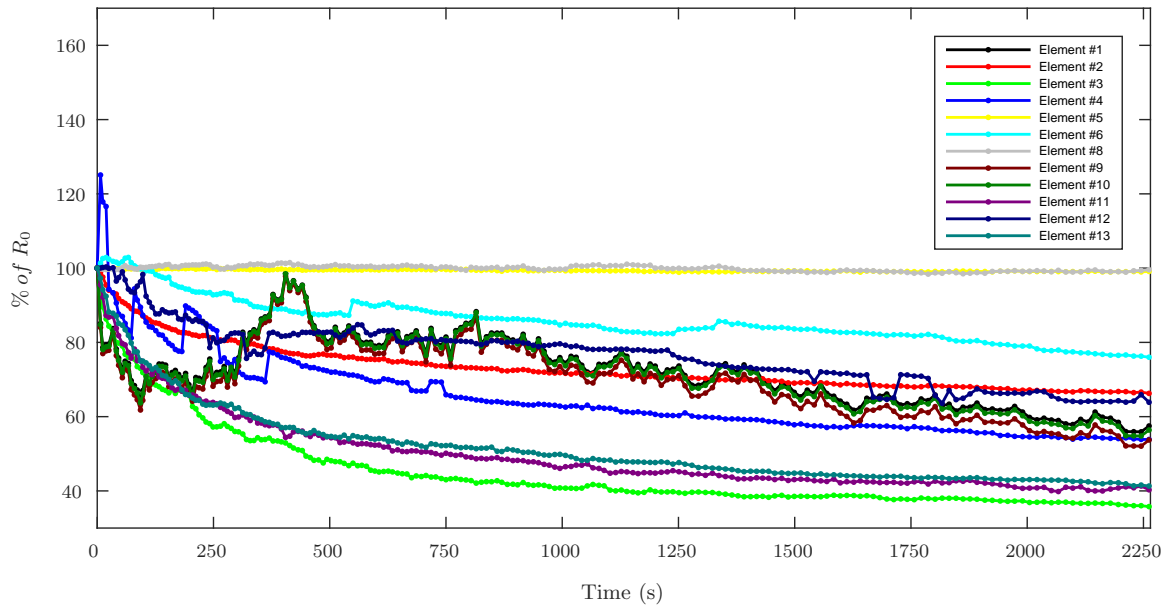


Figure 5.8: Change in resistance under continuous load. Measurements shown for each PANI element under a constant 33.9 N load.

are represented as a percentage of  $R_0$ . Figure 5.9, Figure 5.10, and Figure 5.11 show the change in resistance for a PANI element during incremental continuous loading up to 6.8 N. After this point the response of the elements tends to plateau. A linear trendline is also visible for each element. Although the values of each trendline do not match, it should be noted that the trend lines follow a similar shape for all elements. The multiple values measured for the resistance, during the 60 s period, on each loading step, are plotted. Since all curves for each region of sensors show the same tendencies, element #1 was chosen as an example of external elements, element #13 of middle elements, and element #11 as a central element.

#### 5.5.4 Incremental continuous loading of the entire sensor

The resistance value measured at 1.7 N of applied load ( $R_0$ ) is considered to be 100% of each PANI element's resistance. All other values, measured at different applied pressures, are represented as a percentage of ( $R_0$ ).

Figure 5.12 shows the change in resistance for each PANI element during incremen-

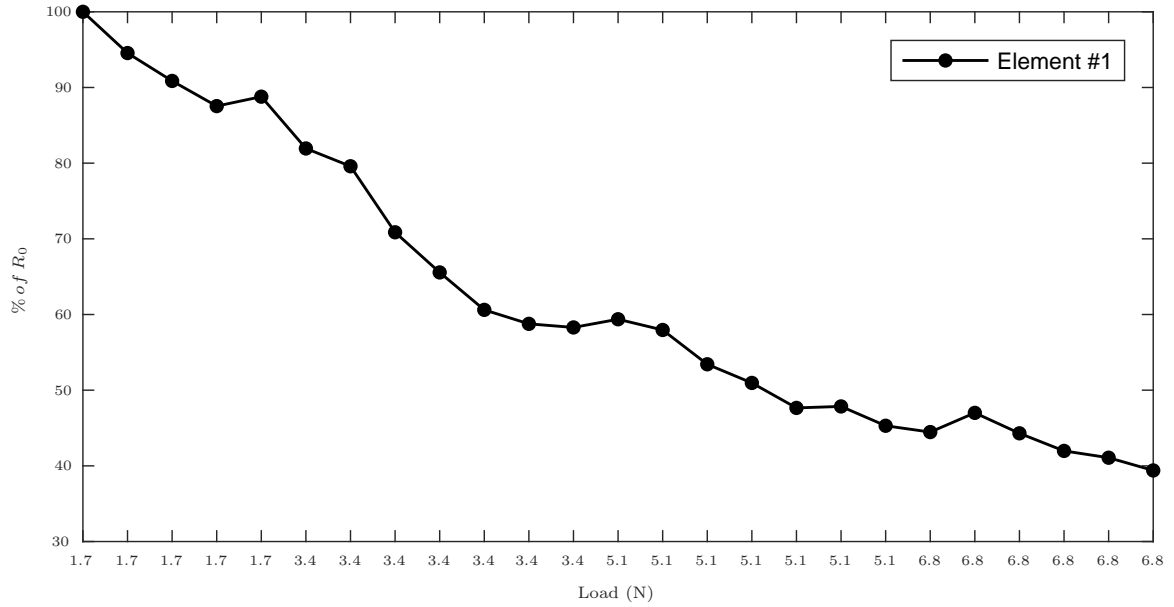


Figure 5.9: Change in resistance, as a function of  $R_0$ , during incremental loading of element #1.

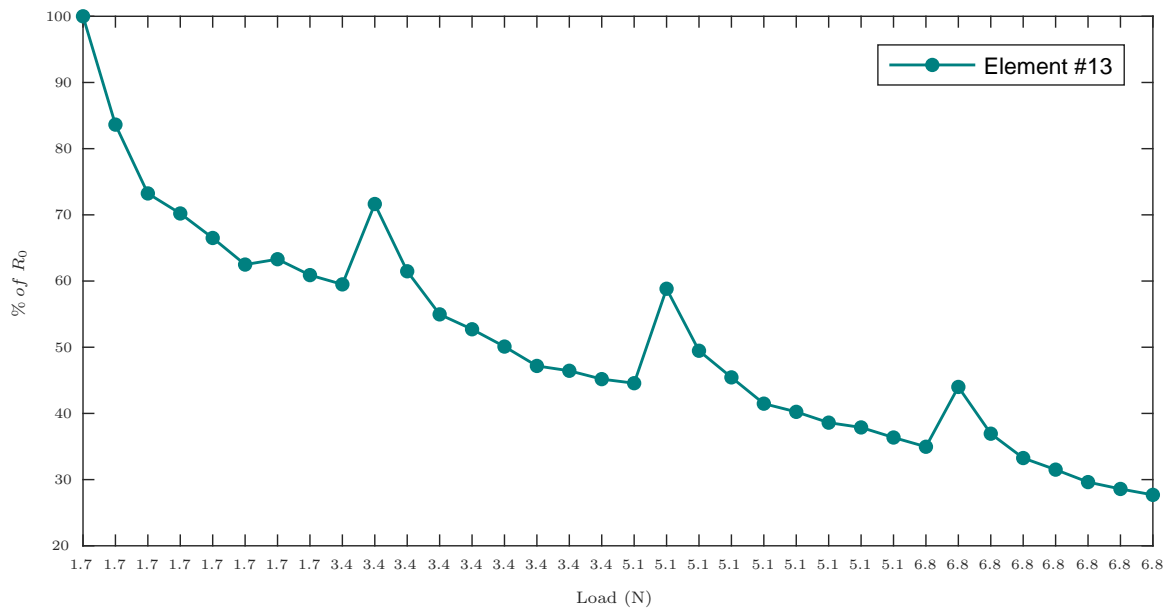


Figure 5.10: Change in resistance, as a function of  $R_0$ , during incremental loading of element #13.

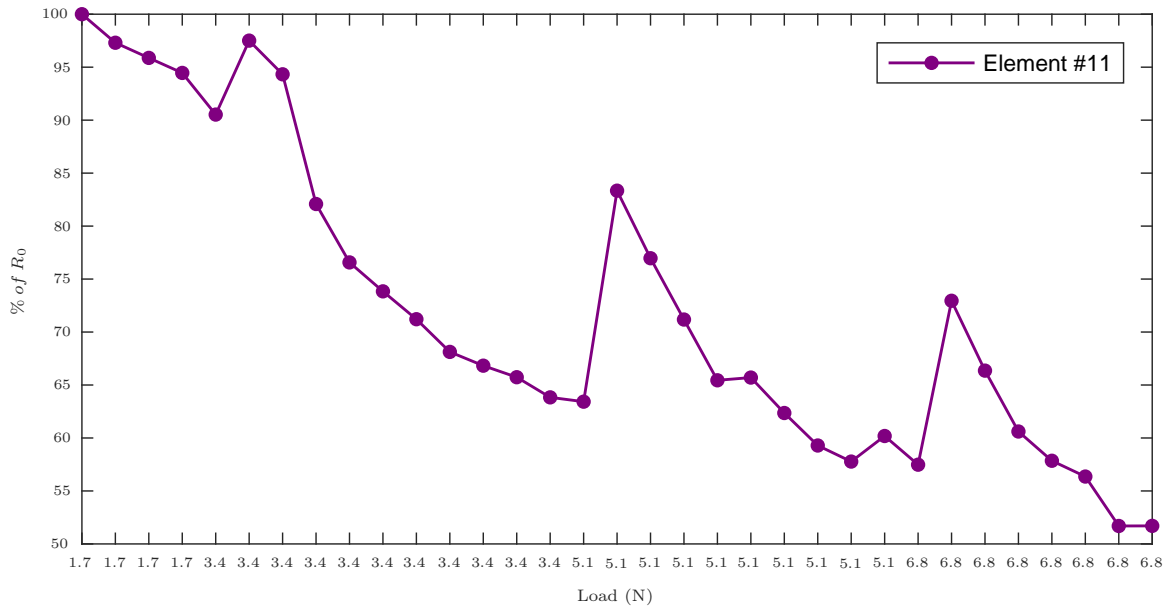


Figure 5.11: Change in resistance, as a function of  $R_0$ , during incremental loading of element #11.

tal continuous loading, with loads applied to the entire sensor using the glenoid sphere. Loads were applied up to 25.42 N, with the base inclined at  $0^\circ$ . Similar to the individual element results, the trendlines are similar for all elements although the values do not match due to the relative position of the elements within the sensor. Since all curves for each region of sensors show the same tendencies, element #7 was chosen as an example of external elements, element #13 of middle elements, and element #11 as a central element.

## 5.6 Signal acquisition and processing

A sample of the GUI output is shown in Figure 5.13, after the calibration the GUI shows the values of the unknown loads. In this case, calibrated in units of cN, which are located to the right of the image.



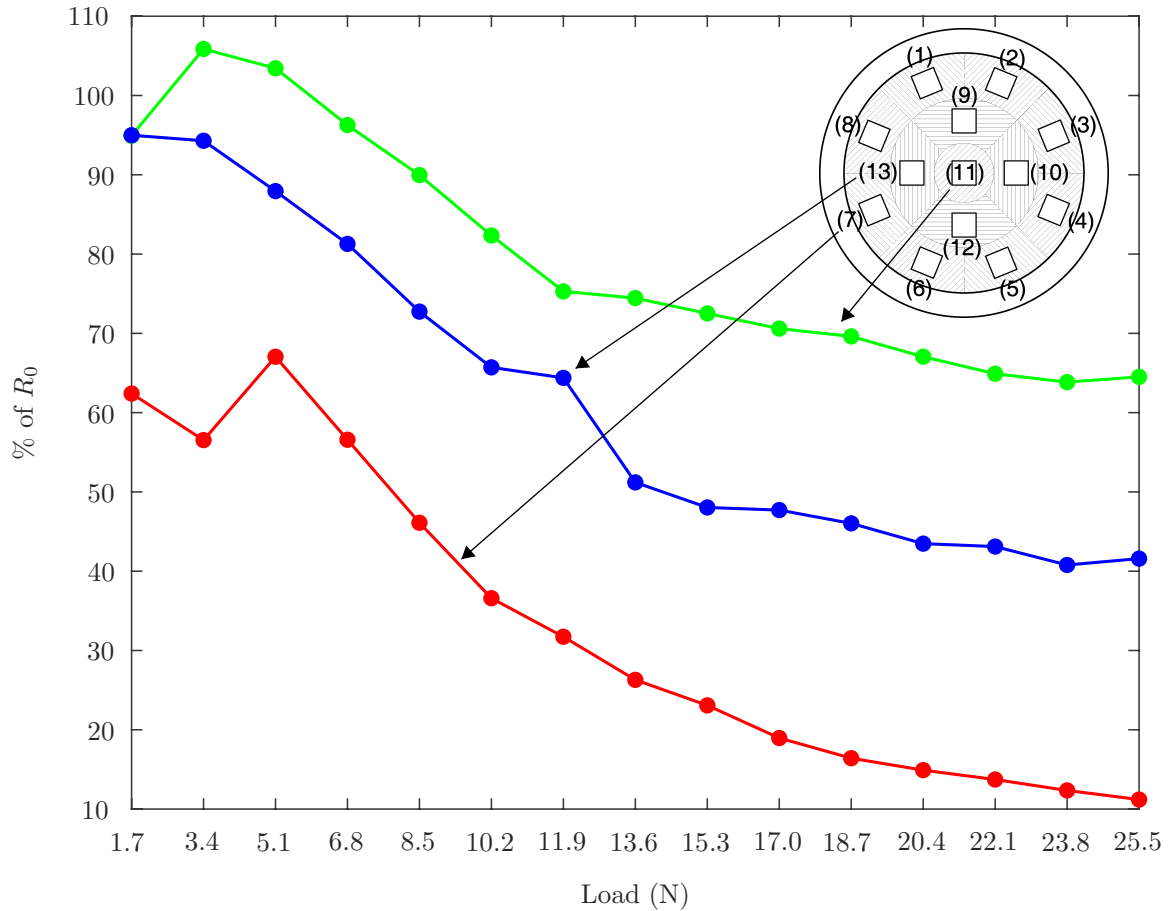


Figure 5.12: Change in resistance, as a function of  $R_0$ , during incremental continuous loading of entire sensor at  $0^\circ$ , with results shown for elements #7, #11, and #13.

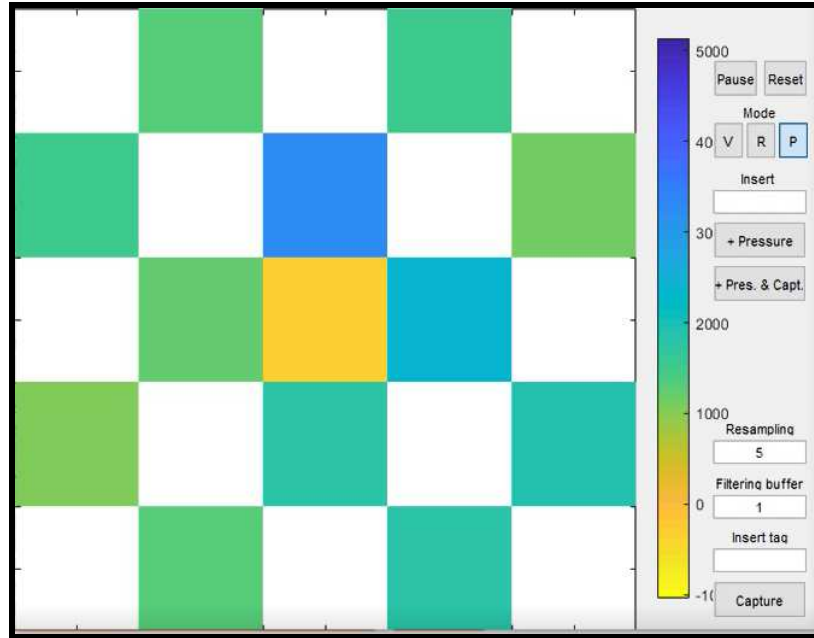


Figure 5.13: Custom GUI developed to display resistance measurements from the 3D joint replacement prosthetic sensor, calibrated in units of cN, showing 13 active PANI elements and the zeroed zones of the  $5 \times 5$  matrix.

## 5.7 Discussion

In the previous chapter, section 4.5 discussed calibration of the flat sensor. These results, specifically those related to cyclic loading, suggested that this test should be carried out first during the sensor calibration to obtain a more stable resistance measurement and to overcome the initial mechanical instabilities observed within the polymers (Falletta et al., 2014). Because a prosthetic glenoid sphere was used for this test and not all the forces were normal to the sensor elements, a 33.9 N force was applied; this was chosen to be greater than the 6.78 N used on the flat sensor.

Figure 5.7 shows the loaded resistance measurements obtained during cyclic loading. These results show that after 16 cycles, the fractional change in PANI's electrical resistance ranges between 0.5 and  $-0.5$ . This is the same range in which the results from the flat sensor were considered stable, occurring after 30 cycles. In the unloaded state, the sensing elements appear to become stable after 25 cycles, as shown in Fig-

ure 5.6. The variation in the resistance measurements is within the range of 0.5 and  $-0.5$  at this point. The fact that the unloaded resistance values take a higher number of cycling loads to stabilize can be attributed to the imperfect connection of the wires rather than the problem of stabilizing of the elements themselves. Element #3 is a good example of this phenomenon, as it shows a high peak between cycles 5 and 7 corresponding to an initial connectivity problem overcome by the applied load.

During continuous load application, shown in Figure 5.8, central element #11 does not present an apparent change in its resistance value. As mentioned, this can be attributed to the fact that this element was located in line with the hole in the glenoid sphere for the insertion of the fastening screw. In the case of the external element #5, it is evident that the glenoid sphere was not perfectly centered during this test, since this element does not show an apparent change in its resistance value. Likewise, it is observed that some exterior elements indicate a relatively large decrease in their resistance values. This further suggests that the glenoid sphere was positioned leaning towards those elements. By not being perfectly centered, the applied load may have caused the sensor to move, causing the final measurement not to stabilize as fast as it did with the flat sensor.

When an unknown load was applied, the same trend could be seen in the GUI, Figure 5.13, the central element #11 presented a value of 0 N, corresponding to the hole in the glenoid sphere. The middle elements showed a darker color compared to the outer ones, indicating that more load was distributed among them. Likewise, elements #9, #10, and #12 showed a darker coloration, as did the outer elements on that side, indicating a slight inclination of the glenoid sphere to the right.

During continuous incremental loading, the same tendency can be seen in all the curves: when the load is applied normal to a particular PANI element, the measured resistance of that element decreases (see Figure 5.9, Figure 5.10, and Figure 5.11). Likewise, all the curves reach a plateau after 6.8 N of the load. A slight increase in

resistance can be seen at the moment when the load increases. This agrees with the trends observed in section 4.4.3 and section 4.4.4 for the flat sensor. Unlike the measurements that were taken for the flat sensor, these curves report data every 5 s, while the previous ones only show the measurements at the end of the 60 s period of stabilization. Furthermore, the calibration of the curved sensor was performed individually for each of the sensing elements, unlike the joint calibration that was used for the flat sensor.

The findings as reported in Figure 5.12 demonstrate the applicability of this technology to quantify the load transfer mechanism through these implant devices. It is interesting to note that there is a marked difference between the 3 levels of the sensorized implant elements for even pure compressive loading at  $0^\circ$ .

One of the problems commonly encountered with sensors of similar design is cross-talk. During the calibration of this curved sensor, no signs of cross-talk between the elements could be seen when the load was perfectly centered and applied normal to one element. From the perspective of design enhancements suggested as future work, it was observed that during the angled tests on the tilting table the metal tip used to apply the load could slip on the inner surface of the sensor. This slippage made it difficult to keep the load centered on the element that was being calibrated.

Another issue that arose during incremental continuous loading of the entire sensor at multiple angles was the separation of the sensor cover from the base and PANI element array. This resulted in exaggerated resistance measurements in the elements opposite to those that were being subjected to a load as the cover separation caused the ground connection to these elements to be broken.

As was noted during the calibration of the flat sensor, section 4.5, the greatest limitation was found to be the fragility of the connections between the PANI and the wires. These connections were unable to provide measurements without being loaded in compression, and if they became too loose the element would disconnect and become

a dead element within the sensor.

Other minor inaccuracies in the data could have been due to a mismatch in the conductivity of the PANI elements in the 3D sensor. For the flat sensor, the heat treatment could be undertaken in an oven, ensuring that all elements were subjected to a uniform temperature. The curved sensor, however, required wiring to be applied prior to the PANI infill. This made it impossible for the sensor to be heat treated continually in an oven. The method of thermal treatment used for the 3D sensor may have resulted in uneven thermal doping of the PANI elements, causing some elements to be more conductive than others.

Overall, the proposed PANI sensor arrays present a stable response and display a good fit with linear relationships to describe the fractional changes in resistance during incrementally applied loads. The calibration of the curved sensor further supports the viability of PANI elements for use in smart-polymer implant sensors.

## **5.8 Chapter summary**

The design, fabrication, characterization, and signal acquisition and processing of a 3D-printed polymer sensor with 13 embedded conductive polyaniline structures were presented in this chapter. Adaptation of the technique for the piezoresistive characterization of the PANI elements embedded in the sensor, in addition to the adaptation of the calibration apparatus, were explained. Results including the fractional change in resistance upon cyclical loading, continuous loading, and incremental loading applied at multiple angles were discussed.

## **List of references**

Della Pina, C., Zappa, E., Busca, G., Sironi, A. and Falletta, E. (2014), 'Electrome-

- chanical properties of polyanilines prepared by two different approaches and their applicability in force measurements', *Sensors and Actuators, B: Chemical* **201**, 395–401.
- Falletta, E., Costa, P., Della Pina, C. and Lanceros-Mendez, S. (2014), 'Development of high sensitive polyaniline based piezoresistive films by conventional and green chemistry approaches', *Sensors and Actuators, A: Physical* **220**, 13–21.
- Holness, F. B. and Price, A. D. (2016), Robotic extrusion processes for direct ink writing of 3D conductive polyaniline structures, in Y. Bar-Cohen and F. Vidal, eds, 'Electroactive Polymer Actuators and Devices (EAPAD) 2016', Vol. 9798 of *SPIE Smart Structures and Materials + Nondestructive Evaluation and Health Monitoring*, SPIE, Bellingham, WA, pp. 97981G–1 – 97981G–8.
- Kang, J. H., Park, C., Scholl, J. A., Brazin, A. H., Holloway, N. M., High, J. W., Lowther, S. E. and Harrison, J. S. (2009), 'Piezoresistive characteristics of single wall carbon nanotube/polyimide nanocomposites', *Journal of Polymer Science B: Physics* **47**(10), 994–1003.

# Chapter 6

## Concluding remarks

### 6.1 Summary of conclusions

This thesis explored the development and use of PANI sensing elements for monitoring applied loads in orthopaedic joint implants. Review of the available literature has identified the need for a better understanding of the forces carried by joint implants, in order to improve their performance under realistic loads caused by the patient's daily activities. The piezoresistive properties of PANI, in addition to other features such as ease of synthesis and bio-compatibility, make it an ideal candidate for load sensing applications in orthopaedic implants. In addition, the use of 3D-printed polymer parts to encase the sensing elements allows for the properties of the actual joint parts to be closely replicated.

The focus of this research was to establish the feasibility and assess the performance of flat and 3D sensors with embedded PANI elements. Testing was carried out using custom loading apparatus and voltage data was collected and analyzed using a custom software interface and circuitry. The key findings and observations from this work have resulted in a number of important conclusions:

- *The multi-material additive manufacturing process for PANI presents a promising*

*method for development of smart-polymer sensors.* The preliminary flat sensor design, as described in section 4.1, was employed to test the viability of the chosen configuration of PANI elements and assess the ability of the sensor to detect loading variations across the sensor surface. The flat sensor provided precise results (less than 8% RMSE) and exhibited a repeatable response under incremental loading. Under constant and cyclic loading, the resistance measurements from the flat sensor stabilized soon after load application, indicating that consistent results can be obtained soon after the onset of loading, once initial mechanical instabilities are overcome.

- *The PANI-embedded flat sensor exhibits a linear trend in the resistance output when subjected to increasing loads.* Although the magnitude of resistance measurements varied across the flat sensor under uniform pressure, the resistance trendline for each element under incremental loading takes the same shape. This suggests that the PANI elements performed in a consistent manner, but were likely subject to variations in the fabrication and wiring of each individual element. Overall, the results from the flat sensor indicate that the embedded PANI elements exhibit a reliable response.
- *The through-thickness sensing mode provides a reliable method of analyzing the response of the PANI elements.*
- *The 3D sensor displays stable, repeatable results, similar to those from the flat sensor.* Overall, the results from the 3D-printed humeral cup sensor were consistent with those expected, and they further verify the feasibility of the PANI sensing method. Variations in the element-by-element response occurred due to the variation of applied loads across the surface, caused by the shape and positioning of the Glenoid sphere used in the joint tests. The effect of concentrated compressive loads on certain elements also resulted in separation of the polymer sensor



cover from the base, and loss of electrical contact at the connections which were not experiencing high compressive loads. This separation resulted in high resistance measurements from the affected elements. However, this effect may be useful for identifying the relative forces across the surface of a realistic humeral cup.

## 6.2 Summary of contributions

The most significant research contributions of this thesis relate to the proposed sensor design, as well as the fabrication and calibration methodologies successfully applied in the work. These contributions are summarized as follows:

- *Novel 3D-printed sensors, consisting of a thermoplastic polymer embedded with PANI sensing elements, are developed and design considerations are provided.* The proposed sensor is based on using PANI's piezoresistive properties to detect load changes during the unidirectional loading of the elements. After calibration, the custom-made software was able to relate the applied load with the corresponding change in resistance and plot the sensor loads in the graphical user interface.
- *The first-ever study using the piezoresistive properties for PANI sensing elements constructed using a novel 3D printing technique.* This thesis presents critical data for relating the resistance changes in the PANI material under unidirectional loads. In particular, the data which reveals the loading range in which the PANI elements display linear behaviour will facilitate the design of diverse sensors that act within the limits of the linearity range.
- *Adaptation of the planar sensor model for use in a hemispherical geometry to replicate the typical humeral cup implant used in reverse total shoulder arthro-*

*plasty*. This adaptation demonstrates a promising sensor manufacturing technique for use in the study of diverse prosthetic designs.

### 6.3 Recommendations for future research

A novel way of harnessing the piezoresistive characteristics of polyaniline is presented in this thesis for the development of 3D-printed implant components with embedded smart-polymer sensors. The aim was to provide an innovative technique for the measurement of the internal forces supported by joint replacement orthopaedic prostheses which use a UHMWPE component. Following from the present research, which confirms the suitability of the proposed PANI sensing method, a number of recommendations for future research are given:

- *Improvements to the piezoresistive characterization described in Chapter 4.* The calibration results could be improved in future tests by using a more accurate device for resistance measurement and load application. During the calibration tests, it was found that the pressure range that can be measured with polyaniline (i.e. the linear range) is below the maximum reactive forces observed in reverse shoulder implant. The measurement range of the PANI elements may be improved through the addition of more sensing elements to further distribute the load and refine the results from those presented in Chapter 5.
- *Improved connections between the sensing elements and the wires.* One of the problems faced when using conductive polymers is their connection to the wires. Although this issue was addressed in Chapter 3, it would be valuable to use a less rigid, silver-filled electrically conductive adhesive to avoid cracking during testing. One possible candidate could be EP3HTSDA-2 (MasterBond, U.S.), a one-part silver filled adhesive.

- *Testing of an array distribution similar to the one discussed in section 2.1.2, showing a central core and four sidewall structures, could be used to discriminate the force direction and magnitude.*

- *Extending the sensing method to different joint designs and practical applications.*

The great advantage of this technology is that it has the potential to be extended for use in any implant that has a component manufactured with UHMWPE. In the future, it will be of great interest to adopt the current technology for more implant designs, to gather performance requirements from implant designers to reflect their views and needs in the design of the sensor arrays. Finally, this new and improved sensor design applications should be tested on cadaveric joints in order to evaluate its ability to monitor forces in a realistic application. The feasibility of insertion of the device, the response time for results processing, and the effectiveness of the resulting graphs for the end user should be evaluated.

# Appendices

# Appendix A

## Curriculum vitae

<b>Name:</b>	Carolina Micolini
<b>Post-Secondary Education and Degrees:</b>	National University of Cordoba Argentina Córdoba, Córdoba, Argentina 2005 – 2013 B.A.Sc. Biomedical Engineering  The University of Western Ontario London, Ontario, Canada 2016 – 2017 M.E.Sc. Biomedical Engineering
<b>Honours and Awards:</b>	Organization of American States (OAS) Regular Program Academic Scholarships (Graduate) Jan – Dec 2016 Jan – Dec 2017
<b>Related Work Experience:</b>	Teaching Assistant The University of Western Ontario ECE 2277A – Digital Logic Systems 2016 – 2017

### Publications:

1. **Micolini, C**, Holness, FC, Johnson JA, & Price, AD, “Assessment of Embedded Conjugated Polymer Sensor Arrays for Potential Load Transmission Measurement in Orthopaedic Implants,” *Sensors* 2017, **17**(12), p. 2767. Available from: MDPI [doi: [10.3390/s17122768](https://doi.org/10.3390/s17122768)]
2. **Micolini, C**, Holness, FC, Johnson, JA, & Price, AD, “Conductive polymer sensor arrays for smart orthopaedic implants,” *SPIE Proceedings 10167, Nanosensors, Biosensors, Info-Tech Sensors and 3D Systems 2017*. Available from: SPIE [doi: [10.1117/12.2260404](https://doi.org/10.1117/12.2260404)].